
CHAPTER 92

Dynamics of Condensed Phase Proton and Electron Transfer Processes

Raymond Kapral, Alessandro Sergi

*Chemical Physics Theory Group, Department of Chemistry,
University of Toronto, Toronto, Canada*

CONTENTS

1.	Introduction	2
2.	Chemical Reaction Rates	2
2.1.	Microscopic Expressions for Rate Constants	2
2.2.	Classical Mechanical Rate Expression	4
2.3.	Blue Moon Ensemble	5
3.	Free Energy Along the Reaction Coordinate	6
3.1.	Imaginary Time Path Integral Molecular Dynamics	6
3.2.	Electron Solvation in Reverse Micelles	8
3.3.	Proton Transfer in Nanoscale Molecular Clusters	10
4.	Adiabatic Reaction Dynamics	13
4.1.	Quantum-Classical Adiabatic Dynamics	13
4.2.	Adiabatic Proton-Transfer Reactions in Solution	15
4.3.	Proton Transfer Dynamics in Nanoclusters	16
5.	Mean Field and Surface Hopping Dynamics	18
5.1.	Mean-Field Method	19
5.2.	Surface-Hopping Dynamics	19
5.3.	Nonadiabatic Proton Transfer in Nanoclusters	20
6.	Quantum-Classical Liouville Equation	21
6.1.	Simulation Algorithm	24
7.	Nonadiabatic Reaction Dynamics	25
7.1.	Quantum-Classical Reactive Flux Correlation Functions	25
7.2.	Two-Level Model for Transfer Reactions	26
7.3.	Two-Level Reaction Simulation Results	28

8. Conclusions	30
References	31

1. INTRODUCTION

Proton and electron transfer reactions are ubiquitous in chemistry and govern many important physical and biological functions [1–3]. In order to understand the mechanisms through which such reactions take place and to determine their rates, one must account for the quantum nature of these transferring particles. This feature provides challenges for theory and simulation because quantum dynamics in many-body environments is difficult to carry out.

The rate constants that characterize the interconversion of chemical species can be computed from a knowledge of reactive flux correlation functions. In this chapter, we sketch the derivation of these microscopic formulas for rate constants that can be used to compute electron and proton transfer rates. For activated chemical rate processes, where chemical reactions take place on timescales that are long compared to typical microscopic relaxation times accessible in computer simulation methods, one must devise schemes for sampling rare reactive events. We discuss one such method, the blue moon ensemble, which can be used to obtain the rate from short time simulations of the dynamics. The reactive flux formalism provides a natural decomposition of the rate constant expression into a transition state theory contribution and a transmission coefficient that accounts for dynamical recrossing events. Because the transition state theory rate depends on the free energy along the reaction coordinate, this quantity is an important ingredient in estimating the reaction rate. We give examples of the computation of the free energy for reactions occurring in bulk condensed phases as well as in materials with nanoscale dimensions such as clusters and micelles.

The main focus of this chapter is on quantum mechanical rate processes, such as those associated with electron and proton transfer processes, and we describe methods for computing rates of these reactions. The methods will be illustrated by considering again simple models for such processes in bulk and cluster environments. The emphasis of this presentation is on the theoretical methods and the basic elements of the physical mechanisms that underlie and govern such processes.

2. CHEMICAL REACTION RATES

A phenomenological description of the dynamics of a chemical reaction $A \rightleftharpoons B$ can be given in terms of the mass action rate law,

$$\frac{d\bar{n}_A(t)}{dt} = -k_f \bar{n}_A(t) + k_r \bar{n}_B(t) \quad (1)$$

where $\bar{n}_A(t)$ and $\bar{n}_B(t)$ are the mean number densities of species A and B , respectively. If we let $\bar{\chi} = \delta\bar{n}_A = \bar{n}_A - n_A^{eq} = -\delta\bar{n}_B = -(\bar{n}_B - n_B^{eq})$ be the deviations of the species densities from their equilibrium values, the rate law takes the form,

$$\frac{d\bar{\chi}}{dt} = -(k_f + k_r)\bar{\chi} \quad (2)$$

Our goals are to determine microscopic expressions for the rate constants and to construct algorithms to compute the forward k_f and reverse $k_r = k_f K_{eq}^{-1}$ (K_{eq} is the equilibrium constant) rate constants by molecular dynamics simulation.

2.1. Microscopic Expressions for Rate Constants

We present a quantum mechanical formulation of reaction rates because our primary interest is in proton and electron transfer processes. However, as we shall see below, the classical limit results can be used in some circumstances to obtain approximations to quantum rates. The rate at which the A and B species interconvert can be determined from the reactive

flux correlation expression for the rate constant [4–6]. To derive the chemical rate law [7, 8], we start from the Heisenberg equation of motion for $\hat{\chi}$, an operator that characterizes the deviation of species A from its equilibrium value,

$$\frac{d\hat{\chi}(t)}{dt} = \frac{i}{\hbar}[\hat{H}, \hat{\chi}(t)] \equiv i\hat{\mathcal{L}}_q\hat{\chi}(t) \quad (3)$$

Here the last equality defines the quantum Liouville operator, $\hat{\mathcal{L}}_q$. We shall discuss suitable choices for such species operators in later sections. We may extract the evolution proportional to $\hat{\chi}(t)$ using projection operator methods [9, 10]. An appropriate projection operator is $\hat{\mathcal{P}}\hat{\mathcal{C}} = \langle \hat{\mathcal{C}}; \hat{\chi} \rangle \langle \hat{\chi}; \hat{\chi} \rangle^{-1} \hat{\chi}$, as $\hat{\mathcal{P}}$ just projects $\hat{\mathcal{C}}$ onto $\hat{\chi}$. The Kubo transformed correlation function is defined as [11]

$$\langle \hat{A}; \hat{B}^\dagger \rangle = \beta^{-1} \int_0^\beta d\lambda \hat{A} e^{-\lambda\hat{H}} \hat{B}^\dagger e^{\lambda\hat{H}} \hat{\rho}_e \quad (4)$$

Here $\hat{\rho}_e$ is the quantum canonical equilibrium density matrix, $\hat{\rho}_e = e^{-\beta\hat{H}} / \text{Tr} e^{-\beta\hat{H}}$. Using the operator identity

$$e^{i\hat{\mathcal{L}}_q t} = \int_0^t d\tau e^{i\hat{\mathcal{L}}_q(t-\tau)} \hat{\mathcal{P}} i\hat{\mathcal{L}}_q e^{i\hat{\mathcal{C}}\hat{\mathcal{L}}_q\tau} + e^{i\hat{\mathcal{C}}\hat{\mathcal{L}}_q t} \quad (5)$$

where $\hat{\mathcal{C}} = 1 - \hat{\mathcal{P}}$, we obtain the generalized Langevin equation for $\hat{\chi}(t)$,

$$\frac{d\hat{\chi}(t)}{dt} = - \int_0^t \tilde{k}(\tau) \hat{\chi}(t - \tau) + \hat{R}(t) \quad (6)$$

where the rate kernel is defined as

$$\tilde{k}(t) = \langle e^{i\hat{\mathcal{C}}\hat{\mathcal{L}}_q t} i\hat{\mathcal{L}}_q \hat{\chi}; i\hat{\mathcal{L}}_q \hat{\chi} \rangle \langle \hat{\chi}; \hat{\chi} \rangle^{-1} \quad (7)$$

The random reactive flux is $\hat{R}(t) = e^{i\hat{\mathcal{C}}\hat{\mathcal{L}}_q t} i\hat{\mathcal{L}}_q \hat{\chi}$. If we average the generalized Langevin equation over an initial nonequilibrium ensemble where $\hat{\chi}$ is fixed, we find the generalized chemical rate law,

$$\frac{d\bar{\chi}(t)}{dt} = - \int_0^t d\tau \tilde{k}(\tau) \bar{\chi}(t - \tau) \quad (8)$$

If the rate kernel decays on a timescale τ_m that is much more rapid than the chemical relaxation time $\tau_{chem} = (k_f + k_r)^{-1}$, then the generalized rate law takes the form of the mass action rate law with

$$k = k_f + k_r = \int_0^\infty d\tau \tilde{k}(\tau) \quad (9)$$

If the projected dynamics in this equation is replaced by ordinary dynamics [6] and the above inequalities on the microscopic and chemical relaxation times apply, the rate coefficient may be written as

$$k = \int_0^{t^*} d\tau k(\tau) = \int_0^{t^*} d\tau \langle e^{i\hat{\mathcal{L}}_q t} i\hat{\mathcal{L}}_q \hat{\chi}; i\hat{\mathcal{L}}_q \hat{\chi} \rangle \langle \hat{\chi}; \hat{\chi} \rangle^{-1} \quad (10)$$

where t^* is a time such that $\tau_m \ll t^* \ll \tau_{chem}$. It is convenient to define the time-dependent rate coefficient as

$$K(t) = k_f(t)(1 + K_{eq}^{-1}) = \int_0^t d\tau k(\tau) = \frac{-1}{i\hbar\beta} \text{Tr}[\hat{\chi}, \hat{\chi}(t)] \hat{\rho}_e \langle \hat{\chi}; \hat{\chi} \rangle^{-1} \quad (11)$$

where we have used the fact that $\hat{\chi}(t) = e^{i\hat{\mathcal{L}}_q t} \hat{\chi}$. We shall consider the calculation of this expression in later sections.

2.2. Classical Mechanical Rate Expression

To formulate the classical statistical mechanical description of chemical reactions, consider a molecular system containing N atoms with Hamiltonian $H = K(p) + V(r)$, where $K(p)$ is the kinetic energy, $V(r)$ is the potential energy, and (p, r) denotes the $6N$ momenta and coordinates defining the phase space of the system.

We suppose that the progress of the reaction can be characterized on a microscopic level by a scalar reaction coordinate $\xi(r)$ that is a function of the positions of the particles in the system. For the reaction $A \rightleftharpoons B$, we assume that a dividing surface at ξ^\ddagger serves to partition the configuration space of the system into two A and B domains that contain the metastable A and B species. (In general, it is not always clear what a suitable choice of a reaction coordinate is for any given problem. There is an active area of research devoted to the development of schemes for the determination of reaction paths and suitable coordinates to describe the reaction [12–16]. Here we assume that such microscopic coordinates are known and show how to compute the rate.) The microscopic variable determining the fraction of systems in the A domain is $\chi(r) = n_A(r) - \langle n_A(r) \rangle = \theta[\xi^\ddagger - \xi(r)] - n_A^{eq}$, where θ is the Heaviside function. The angular brackets denote an equilibrium canonical average, $\langle \dots \rangle = Q^{-1} \int dr dp \exp\{-\beta H\} \dots$, where Q is the partition function and n_A^{eq} is the equilibrium density of species A . Likewise, the fraction of systems in the B domain is $n_B(r) = \theta(\xi(r) - \xi^\ddagger)$. The time rate of change of $n_A(r)$ is

$$\dot{n}_A(r) = -\dot{\xi}(r)\delta[\xi(r) - \xi^\ddagger] \quad (12)$$

The time-dependent forward rate coefficient can be expressed in terms of the equilibrium correlation function of the initial flux of A with the B species density at time t as [4]

$$k_f(t) = \frac{1}{n_A^{eq}} \langle \dot{n}_A(r) n_A(r, t) \rangle = \frac{1}{n_A^{eq}} \langle \dot{\xi}\delta[\xi(r) - \xi^\ddagger] \theta[\xi[r(t)] - \xi^\ddagger] \rangle \quad (13)$$

For an activated rate process, the reactive flux correlation function will decay rapidly initially, followed by a much slower decay that occurs on the timescale of the slow chemical interconversion process. The rate constant can be determined from the ‘‘plateau’’ value established during the slow decay of this time-dependent rate coefficient [6, 7].

Static and dynamic contributions to the rate coefficient can be defined by multiplying and dividing each term on the right-hand side of Eq. (13) by $\langle \delta[\xi(r) - \xi^\ddagger] \rangle$ to obtain

$$\begin{aligned} k_f(t) &= \left\{ \frac{\langle \dot{\xi}\delta[\xi(r) - \xi^\ddagger] \theta[\xi(r(t)) - \xi^\ddagger] \rangle}{\langle \delta[\xi(r) - \xi^\ddagger] \rangle} \right\} \left\{ \frac{\langle \delta[\xi(r) - \xi^\ddagger] \rangle}{n_A^{eq}} \right\} \\ &= \langle \dot{\xi}\theta[\xi[r(t)] - \xi^\ddagger] \rangle_{\xi^\ddagger}^{cd} \left\{ \frac{e^{-\beta W(\xi^\ddagger)}}{\int_{\xi' < \xi^\ddagger} d\xi' e^{-\beta W(\xi')}} \right\} \end{aligned} \quad (14)$$

where $\langle \dots \rangle_{\xi^\ddagger}^{cd}$ defines an average conditional on $\xi(r) = \xi^\ddagger$,

$$\langle \dots \rangle_{\xi'}^{cd} = \frac{\langle \dots \delta[\xi(r) - \xi'] \rangle}{\langle \delta[\xi(r) - \xi'] \rangle} \quad (15)$$

In writing the second factor in Eq. (14), we used the fact that the equilibrium average $\langle \delta[\xi(r) - \xi^\ddagger] \rangle = P(\xi^\ddagger)$ is the probability density of finding the value $\xi(r) = \xi^\ddagger$ of the reaction coordinate. The free energy $W(\xi')$ associated with the reaction coordinate is defined by $W(\xi') = -\beta^{-1} \ln[P(\xi')/P_u]$, where P_u is a uniform probability density of ξ' . Typically, the free energy will have the form shown schematically in Fig. 1. A high free energy barrier at $\xi = \xi^\ddagger$ separates the metastable reactant and product states. The equilibrium density of species A is

$$n_A^{eq} = \langle \theta[\xi^\ddagger - \xi(r)] \rangle = \int_{\xi' < \xi^\ddagger} d\xi' P(\xi') \quad (16)$$

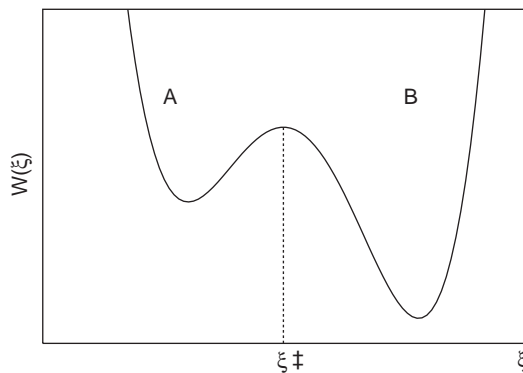


Figure 1. Schematic representation of the free energy versus ξ showing the free energy maximum at $\xi = \xi^\ddagger$ and specification of the A and B domains.

The time-dependent transmission coefficient $\kappa(t)$ is defined as $\kappa(t) = k_f(t)/k_f^{\text{TST}}$, where the transition state theory value of the rate constant is given by the limit $t \rightarrow 0_+$ of Eq. (13) as [5]

$$k_f^{\text{TST}} = \frac{1}{n_A^{\text{eq}}} \langle \dot{\xi} \delta(\xi(r) - \xi^\ddagger) \theta(\dot{\xi}) \rangle \quad (17)$$

The transmission coefficient $\kappa(t)$ measures the deviations from k_f^{TST} due to dynamical barrier recrossing events.

2.3. Blue Moon Ensemble

From this discussion, we see that the calculation of the rate coefficient requires the determination of conditional averages depending on specific values of the reaction coordinate. The ensemble of such configurations, which are visited “once in a blue moon,” is termed the blue moon ensemble [17]. In the blue moon ensemble method, conditional averages of observables depending only on configuration space variables can be computed by applying holonomic constraints to the equations of motion. For the rate problem, while the value ξ^\ddagger we wish to sample is rare in the original ensemble, only configurations with $\xi = \xi^\ddagger$ are sampled in the ξ -constrained ensemble. This is illustrated schematically in Fig. 2. In the blue moon ensemble, conditional averages are related to constrained averages by (here we consider the case of a single constraint but generalization to other situations is straightforward [17])

$$\langle A(r) \rangle_{\xi'}^{cd} = \frac{\langle A(r) \delta[\xi(r) - \xi'] \rangle}{\langle \delta[\xi(r) - \xi'] \rangle} = \frac{\langle |Z|^{-1/2} A(r) \rangle_{\xi'}}{\langle |Z|^{-1/2} \rangle_{\xi'}} \quad (18)$$

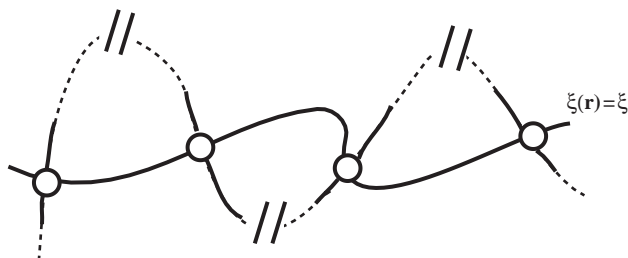


Figure 2. Schematic representation of the sampling procedure in the blue moon ensemble. The bold line depicts the constrained $[\xi(r) = \xi']$ dynamical evolution in phase space. The unconstrained natural evolution of the system is shown as a dashed line. The open circles represent common points in configuration space, which are the initial conditions of the activated trajectory sampling. These points are not real crossings in phase space, as the two trajectories differ in momentum space. Breaks in the dashed line denote long segments in the natural trajectory and indicate that “crossings” are rare events. The dynamics represented by the solid line segments of the unconstrained trajectory close to the crossing points yield the information needed to compute averages.

where the observable $A(r)$ is any function of the configuration space coordinates,

$$Z = \sum_{i=1}^N \frac{1}{m_i} \frac{\partial \sigma}{\partial r_i} \cdot \frac{\partial \sigma}{\partial r_i} \quad (19)$$

with $\sigma = \xi(r) - \xi'$ and $\langle \dots \rangle_{\xi'}$ denotes an average over the constrained ensemble with $\xi = \xi'$. Equation (18) allows one to estimate the *conditional* average on the left-hand side in terms of averages in the *constrained* ensemble, which is statistically advantageous.

In a similar manner, any time correlation function of conditional averages may be written in terms of constrained averages as

$$\frac{\langle A(r, p)B[r(t), p(t)]\delta[\xi(r) - \xi'] \rangle}{\langle \delta(\xi(r) - \xi') \rangle} = \frac{\langle |Z|^{-1/2} A(r, p)B[r(t), p(t)] \rangle_{\xi'}}{\langle |Z|^{-1/2} \rangle_{\xi'}} \quad (20)$$

The $|Z|$ factors [18, 19] in these equations arise from the need to unbiased the momentum distribution, which is obtained from the constrained dynamics. When Newton's equations of motion are integrated with holonomic constraints [20], both σ and $\dot{\sigma}$ are constrained and this distorts the momentum distribution.

3. FREE ENERGY ALONG THE REACTION COORDINATE

Knowledge of the free energy along the reaction coordinate is important for understanding the mechanisms of condensed phase reactions. From the previous section, we saw that it enters the reactive flux formula for the rate coefficient; it also is an important factor in the transition state theory approximation to the rate constant.

The free energy $W(\xi')$ is the reversible work needed to bring the system from a given reference state to $\xi = \xi'$. The thermodynamic force,

$$F(\xi') = -\frac{dW(\xi')}{d\xi'} \quad (21)$$

can be expressed as the conditional average of $\partial H/\partial \xi$. If we perform the derivative in Eq. (21), we find

$$\begin{aligned} F(\xi') &= -\frac{\langle \frac{\partial H}{\partial \xi} \delta[\xi(r) - \xi'] \rangle}{\langle \delta(\xi(r) - \xi') \rangle} = \frac{\langle \left(\beta^{-1} \frac{\partial}{\partial \xi} \ln |J| - \frac{\partial V}{\partial \xi} \right) \delta[\xi(r) - \xi'] \rangle}{\langle \delta(\xi(r) - \xi') \rangle} \\ &\equiv \frac{\langle \widehat{F} \delta[\xi(r) - \xi'] \rangle}{\langle \delta[\xi(r) - \xi'] \rangle} = \frac{\langle Z^{-1/2} \widehat{F} \rangle_{\xi'}}{\langle Z^{-1/2} \rangle_{\xi'}} \end{aligned} \quad (22)$$

where $|J|$ is the Jacobian of the transformation $r \leftrightarrow u = (\sigma, q)$ from coordinates r to the constraint $\sigma = \xi(r) - \xi'$ and a set of remaining coordinates q . The quantity \widehat{F} whose conditional average determines the mean force is the sum of two terms: the first term, $\beta^{-1} \frac{\partial}{\partial \xi} \ln |J|$, represents the apparent forces acting on the system due to the use of generalized (noninertial) coordinates, and the second term, $-\partial V/\partial \xi$, corresponds to the force coming from the potential V . Thus, the thermodynamic force can be determined from a conditional average, which can be computed numerically using the blue moon ensemble [see the last equality of Eq. (22)]. Another expression that does not require the computation of the Jacobian and the ξ derivative of the potential has been derived [21]. The thermodynamic integration of $F(\xi')$ over ξ' will yield the potential of mean force.

3.1. Imaginary Time Path Integral Molecular Dynamics

In proton and electron transfer processes, the quantum character of the transferring particle cannot be neglected although, in many circumstances, the environment in which the reaction occurs can be treated classically. Equilibrium properties such as the free energy along the

reaction coordinate for quantum activated processes can be computed using Feynman's path integral approach to quantum mechanics in imaginary time [22]. In this representation of quantum mechanics, quantum particles are mapped onto closed paths $r(t)$ in imaginary time t , $0 \leq t \leq \beta\hbar$. To see this isomorphism, consider a single quantum particle of mass m with coordinate and momentum operators \hat{r} and \hat{p} , respectively. The Hamiltonian operator is

$$\hat{H} = \frac{\hat{p}^2}{2m} + \hat{V}(\hat{r}) \quad (23)$$

where \hat{V} is the potential energy operator. The path integral formalism is derived by evaluating the trace in the definition of the quantum canonical partition function $Z_Q = \text{Tr} \exp[-\beta\hat{H}]$ in the coordinate representation,

$$Z_Q = \int dr \langle r | e^{-\beta(\frac{\hat{p}^2}{2m} + \hat{V}(\hat{r}))} | r \rangle \quad (24)$$

Using the Trotter formula, this can be rewritten as

$$Z_Q = \lim_{P \rightarrow \infty} \int dr \langle r | \left[e^{-\frac{\beta}{2P}\hat{V}(\hat{r})} e^{-\frac{\beta}{P}\frac{\hat{p}^2}{2m}} e^{-\frac{\beta}{2P}\hat{V}(\hat{r})} \right]^P | r \rangle \quad (25)$$

This equation involves the product of P operators. One can insert $P - 1$ identity operators in the coordinate basis $\hat{I} = \int dr |r\rangle \langle r|$ to obtain

$$Z_Q = \int \prod_{i=1}^P dr_i \left[\prod_{i=1}^P \langle r_i | e^{-\frac{\beta}{2P}\hat{V}(\hat{r})} e^{-\frac{\beta}{P}\frac{\hat{p}^2}{2m}} e^{-\frac{\beta}{2P}\hat{V}(\hat{r})} | r_{i+1} \rangle \right] \quad (26)$$

where, because of the trace, the condition $r_{P+1} = r_P$ must be imposed. The matrix element has the form,

$$\langle r_i | e^{-\frac{\beta}{2P}\hat{V}(\hat{r})} e^{-\frac{\beta}{P}\frac{\hat{p}^2}{2m}} e^{-\frac{\beta}{2P}\hat{V}(\hat{r})} | r_{i+1} \rangle = e^{-\frac{\beta}{2P}V(r_i)} \langle r_i | e^{-\frac{\beta}{P}\frac{\hat{p}^2}{2m}} | r_{i+1} \rangle e^{-\frac{\beta}{2P}V(r_{i+1})} \quad (27)$$

The coordinate matrix elements of the kinetic energy operator $\hat{p}^2/(2m)$ can be evaluated by inserting the identity operator in terms of momentum eigenstates, $\hat{I} = \int dp |p\rangle \langle p|$, using the scalar product between coordinate and momentum eigenstates $\langle r | p \rangle = (2\pi\hbar)^{-1/2} \exp[ipr/\hbar]$, and performing the resulting gaussian momentum integral. One obtains

$$\langle r_i | e^{-\frac{\beta}{P}\frac{\hat{p}^2}{2m}} | r_{i+1} \rangle = \left(\frac{mP}{2\pi\beta\hbar^2} \right)^{1/2} \exp \left[-\frac{mP}{2\beta\hbar^2} (r_{i+1} - r_i)^2 \right] \quad (28)$$

With this result, the path integral expression for the canonical partition function becomes

$$Z_Q = \lim_{P \rightarrow \infty} \left(\frac{mP}{2\pi\beta\hbar^2} \right)^{1/2} \int \prod_{i=1}^P dr_i e^{-\sum_{i=1}^P \left[\frac{mP}{2\beta\hbar^2} (r_{i+1} - r_i)^2 + \frac{\beta}{P} V(r_i) \right]} \quad (29)$$

In simulations, a finite number P of beads is chosen. Equation (29) is the starting point for a classical isomorphism: the single quantum particle with coordinate r is mapped to a closed or *ring polymer* with P beads with coordinates r_i [23]. The configurational statistics of the polymer is governed by the effective potential,

$$V_{eff}(r) = \frac{Pm}{2(\beta\hbar)^2} \sum_{i=1}^P (r_{i+1} - r_i)^2 + \frac{1}{P} \sum_{i=1}^P V(r_i) \quad (30)$$

The problem is then reduced to sampling from a classical canonical distribution involving V_{eff} . In molecular dynamics, this can be achieved by defining the Hamiltonian $H_{eff} = \sum_{i=1}^P (1/2)m_{eff}\dot{r}_i^2 + V_{eff}(r_i)$, where m_{eff} is an arbitrary mass assigned to the polymer beads. The number of polymer beads P enters into the definition of the effective potential V_{eff} in two different ways: it scales the magnitude of the interaction potential acting on the quantum particle (the higher P the smaller this effect); and it determines the harmonic spring constant

$k_{\text{eff}} = Pm/[2(\beta\hbar)^2]$, which represents quantum dispersion effects; it is stiffer for higher P . This stiffness makes it difficult to obtain an ergodic sampling of the dynamics. Moreover, the larger P , the larger the number of degrees of freedom one must integrate numerically. Thus, although a very large P is desirable to represent quantum effects accurately and calculate averages correctly, in practice a compromise is needed.

This formulation can be generalized easily to a single quantum particle interacting with a bath of classical particles. In this case, the bath particles are simply described by a single polymer bead, and the potential operator $\widehat{V}_{\text{eff}}(r, R)$ is

$$\widehat{V}_{\text{eff}}(r, R) = V_{\text{eff}}(r) + V_c(r, R) + V_b(R) \quad (31)$$

where $V_b(R)$ describes the energy of the bath of classical particles with coordinates R and $V_c(r, R)$ the interaction between the quantum particle (polymer beads) and the classical bath particles. Again, the Hamiltonian H_{eff} used for molecular dynamics sampling must be augmented by the kinetic energy of the classical particles: $\sum_{j=1}^N (1/2)M_j\dot{R}_j^2$, where N is the number of classical particles and M_j are their masses. Extension to a bath of distinguishable quantum particles is straightforward. If the bath particles are indistinguishable, then sampling is more difficult.

The path integral approach has been used by Gillan [24] to study rates of quantum activated processes with the centroid density as a reaction coordinate. This approach has been developed extensively by Voth [25]. In this scheme, the reaction coordinate is identified with the position of the centroid of the quantum path \bar{r}_c

$$\xi(r) \equiv \bar{r}_c = \frac{1}{P} \sum_{i=1}^P r_i \quad (32)$$

With this definition of the reaction coordinate and the isomorphism to a classical ring polymer, the classical blue moon ensemble can be applied straightforwardly to compute the free energy, $W(\xi)$, using the relations given earlier specialized to the centroid reaction coordinate,

$$e^{-\beta W(\xi^\ddagger)} \propto \langle \delta[\xi(r) - \xi^\ddagger] \rangle \propto \int dR \prod_{i=1}^P dr_i \delta[\xi(r) - \xi^\ddagger] e^{-\beta V_{\text{eff}}(r, R)} \quad (33)$$

These equations form the basis for the calculation of free energy in transfer processes of a quantum particle embedded in a bath of classical degrees of freedom.

3.2. Electron Solvation in Reverse Micelles

As the first example of the computation of the free energy along a reaction coordinate, we consider the solvation of an electron in aqueous reverse micelle [26]. Reverse micelles are formed when surfactants are dissolved in neat organic solvents or in organic phases containing small amounts of water. In the latter case, the reverse micelles are roughly spherical pools of water surrounded by the polar head groups of the surfactant molecules. The water/surfactant ratio determines the micellar size and properties. Reverse micelles are useful as microreactors for chemical and biochemical reactions [27, 28]. Chemical reactions can be carried out in confined environments where the encounter rates between species are rapid compared to those in the bulk phases and, because polar and nonpolar environments are in close proximity, reactions that are difficult to achieve in bulk homogeneous environments may be carried out efficiently.

Many of the unusual properties of reverse micelles have their origin in the nature of the water phase within the micelle. Micellar water is often partitioned into two zones corresponding to *surface* water, that is, water tightly bound to the surfactant head groups and associated counterions, and *bulk* water in the center of the micelle. The size of the reverse micelle and the relative amounts of these two water phases can be tuned by changing the ratio $w_0 = [\text{water}]/[\text{surfactant}]$. The water structure within the micelles is often studied through its interactions with probe species and solvated electrons, produced by radiolysis or other means. Such studies have provided insight into the nature of the reverse micellar

structure. Chemical and biochemical reactions in reverse micelles often involve electron transfer processes.

Molecular-level studies of electron solvation in reverse micelles are difficult. The micellar structure is complex because it involves the formation of the micelle by arrangement of the surfactant head groups around the water pool. The configurational degrees of freedom of the tail groups play an important part in the stabilization of the micelle. Microscopic studies of micelles in which the full structure of the surfactant molecules has been taken into account have been carried out [29]. Faeder and Ladanyi [30] constructed a simple model for the surfactant molecules to study micellar structure. The tail groups were neglected by supposing that the interior of the micelle was confined by a spherical potential. The surfactant head groups extended into the water pool and were free to move on the micellar surface. This model mimics micelles formed using the sodium bis(2-ethylhexyl)sulfosuccinate (AOT) surfactant in dilute mixtures of water in nonpolar solvents. For this model, the effects of the hydrophobic portions of the amphiphiles and the nonpolar phase are taken into account through a confining potential that gives the micelle a spherical structure with radius R . The SO_3^- head groups and Na^+ counter ions of the surfactant molecules are taken into account explicitly.

Electron solvation in reverse micelles was studied by treating the electron by an imaginary time path integral representation [22]. The model of Faeder and Ladanyi was used for the micelle. Figure 3 shows a molecular configuration for the $w_0 = 7.5$ micelle with a solvated electron-polymer in the interior of the aqueous pool.

The coupling of the electron to the other molecules in the micelle was described by the potential V_{es} , which has three main contributions, $V_{es} = V_{e-w} + V_{e-\text{SO}_3^-} + V_{e-\text{Na}^+}$. Here V_{e-w} is the electron-water potential, which was taken from the pseudopotential model of Schnitker and Rossky [31]. Assuming a united atom model for SO_3^- groups, the electron- SO_3^- interaction $V_{e-\text{SO}_3^-}$ was taken to consist of pairwise additive Coulombic terms. For the electron-counter ion contribution $V_{e-\text{Na}^+}$, the local pseudopotential form given in Bachelet et al. [32] was adopted. The potential energy among the classical particles V_{cl} was taken from Faeder and Ladanyi [30], except for the water-water interactions where the SPC model

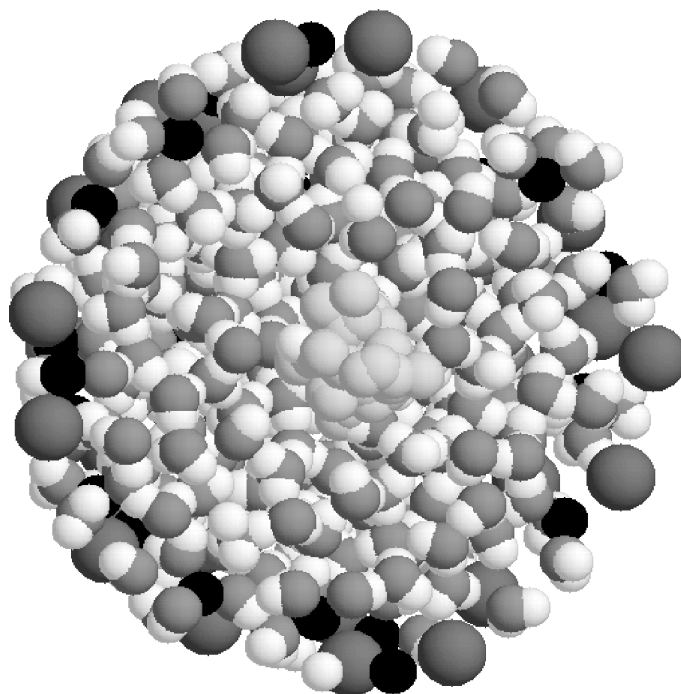


Figure 3. Cross section of the micelle showing a molecular configuration of the internal structure of a $w_0 = 7.5$ aqueous reverse micelle with the electron-polymer (light gray) solvated in the central (bulk water) part of the aggregate. The counter ion and surfactant head groups at the micelle boundary are rendered in black and dark gray shading, respectively.

was employed [33]. To sample the phase space of this system governed by an effective potential V_{eff} of the form in Eq. (31), the multiple time step integration of Newton's equation of motion [34] and the staging algorithm [35] were implemented. A chain [36] of Nosé-Hoover thermostats was used to simulate canonical dynamics. Chains consisting of three Nosé-Hoover thermostats set at $T = 298$ K were coupled to each Cartesian coordinate of the polymer–electron; an additional chain was also attached to the rest of the classical particles.

We now describe the results of simulations of electron solvation on micelles whose sizes lie in the nanometer range and were characterized by the ratios $w_0 = 3$ ($R = 13.2$ Å) and 7.5 ($R = 19.4$ Å). To investigate the solvation of the electron in the micelle, the electron centroid,

$$r_c = \frac{1}{\beta\hbar} \int_0^{\beta\hbar} r(t) dt = \frac{1}{P} \sum_{i=1}^P r_i \quad (34)$$

was fixed at a given distance from the micelle center by a holonomic constraint. The free energy was computed as a function of this distance from the micelle center from MD simulations of the constrained equations of motion using the SHAKE algorithm [37]. The centroid free energies $W_C(r)$ for two micelle sizes are presented in Fig. 4. One can see that the most favorable radial positions for the electron solvation in $w_0 = 3$ and $w_0 = 7.5$ micelles correspond to $r_c \approx 2$ and ≈ 5.5 Å, respectively. A rough estimate of the actual radial domain within which the electron centroid is likely to be found can be obtained by considering regions where $W_C(r)$ remains comparable to normal thermal energies. For $w_0 = 3.5$, this region is a spherical shell defined by $0.5 \leq r \leq 3$ Å, whereas for $w_0 = 7.5$ the corresponding shell is shifted and is defined by $3.5 \leq r \leq 7$ Å. These calculations show that the electron is preferentially solvated in the interior of the micelle. Additional, more detailed, information on the electron solvation structure has been obtained from such path integral simulation studies [26].

3.3. Proton Transfer in Nanoscale Molecular Clusters

Clusters are an interesting environment for the study of solvent influenced reactions. The competition between bulk and surface solvation forces influences the reaction dynamics and modifies the reaction rate. We present results for the proton transfer free energy in large liquid clusters whose linear dimensions are in the nanometer range [38]. Such clusters lie between the microscopic and macroscopic domains and possess unusual properties. We examine the mechanism for proton transfer in a strongly hydrogen bonded proton–ion complex in a cluster that consists of a classical solvent of polar diatomic molecules. The activation free energy in strongly hydrogen bonded systems arises almost exclusively from solvent effects and proton transfer provides a sensitive probe of cluster solvent structure and dynamics.

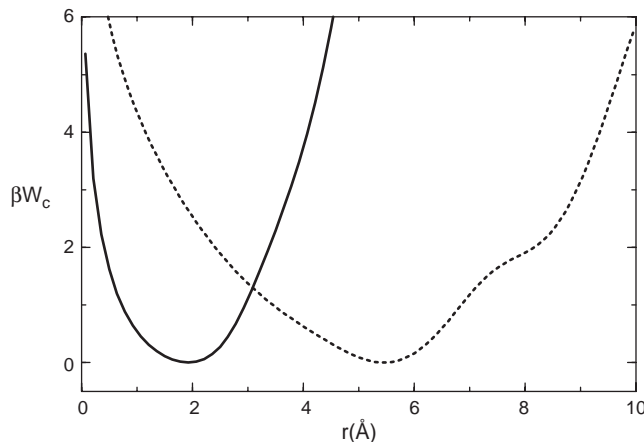
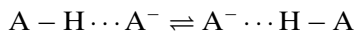


Figure 4. Free energy as a function of the position of the electron centroid for different micelle sizes: $w_0 = 3$ (solid line); $w_0 = 7.5$ (dot-dashed line). The zeros of the mean potential were arbitrarily set at the curve minima.

The proton transfer is assumed to take place between two A^- ions in a proton-ion complex,



embedded in a cluster of N diatomic molecules composing the solvent. The two ions are fixed at $R_{1,2} = (0, 0, \pm 1.3)$ Å. The solvent diatomic molecules have a dipole moment of $\mu = 5.0$ D. The interactions among the cluster solvent molecules, as well as those between the A^- ions and the solvent, arise from Lennard-Jones and Coulomb forces. The proton interacts with the solvent via Coulomb forces. The proton-ion potential was constructed to model strongly hydrogen bonded systems and has a negligibly small intrinsic barrier. Simulations were carried out for clusters with $N = 40$ solvent molecules at a temperature of 220 K, where the cluster (solvent plus proton-ion complex) is in the liquid state.

The calculations of the proton free energy along the reaction coordinate were performed by treating the proton quantum mechanically and the solvent ions classically as discussed earlier for electron solvation. The equilibrium averages involved in the computation of the free energy were estimated from time averages over trajectories of a system with the Hamiltonian obtained by using fictitious masses for the polymer beads representing the quantum proton. Sampling from a canonical distribution was carried out using Nosé-Hoover dynamics [39, 40]. In order to achieve a proper thermalization of the proton degrees of freedom, a second thermostat, acting exclusively on the proton-polymer degrees of freedom, was included [41].

The free energy was computed using the formulas given earlier, again choosing the z coordinate of the centroid of the proton quantum path in imaginary time, $\bar{z} = \xi(i\hbar t)$ [24, 42, 43] as the reaction coordinate. The free energy as a function of z is shown in Fig. 5. The calculations were carried out using the constrained dynamics method described above, namely, the mean force was calculated by constraining \bar{z} and the free energy was obtained by integration of the average force acting on \bar{z} . The activation energy (barrier height) is estimated to be $W(0) = 4.94$ kT (2.15 K cal/mol) and the minima of the free energy profile are located at $z_{min} = \pm 0.68$ Å. Because the intrinsic (bare) barrier is negligibly small (0.2 K cal/mol), essentially all of the activation free energy arises from solvent effects. Figure 5 also shows the free energy determined from a histogram of $P(\xi)$ obtained in a 2 ns unconstrained MD run.

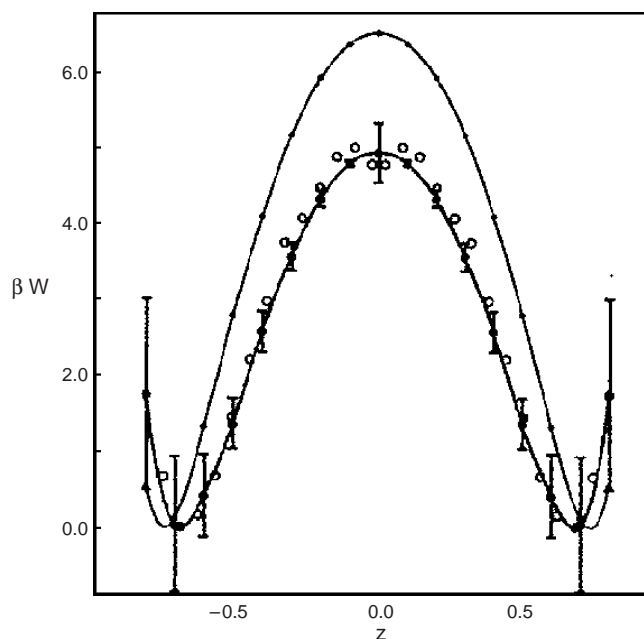


Figure 5. Free energy profiles for the proton transfer reaction. The large dots correspond to the results obtained by integration of the mean force for the quantum proton. The heavy solid line is the interpolation curve to the above results. The open circles are the results from the unconstrained calculation for the quantum proton. The smaller dots and thin line correspond to the results obtained by integration of the mean force for the classical proton.

For comparison, the free energy treating the proton as a classical particle was also computed. These classical results, obtained from a series of constrained MD runs, are shown in Fig. 5 as a thin solid line. The activation energy is 6.56 kT (2.79 K cal/mol), and the minima are located at ± 0.74 Å. These differences can be attributed to the delocalization of the proton charge density in the quantum system, which influences how the proton interacts with the solvent [41], and not to tunneling through the bare barrier as in the case of weakly hydrogen bonded systems [42, 43].

One may contrast these cluster results with the analogous results obtained for bulk phase systems with similar potential models [41, 44]. Although the temperatures are different (250 K for the bulk phase simulations and 220 K for the cluster) (the temperature range in which a liquid cluster shows no evaporation over the timescale of the simulation dynamics is restricted), we can compare the barrier heights in units of kT. For the same solvent with a molecular dipole moment of $\mu = 5.0$ D, the bulk phase free energy barrier height was 2.63 kT, much smaller than that found in the cluster. In both cases, the intrinsic barrier in the strongly bonded proton-ion complex is negligible. This model did not include vibrations of the complex, which can lead to substantial changes in the proton transfer dynamics [45].

The solvent polarization reaction coordinate provides another view of the proton transfer activation free energy. The solvent polarization is given by [44, 46–48],

$$\xi(R) = \Delta E(R) = \sum_{i,a} z_a e \left(\frac{1}{|r_i^a - u|} - \frac{1}{|r_i^a - u'|} \right) \quad (35)$$

The points u and u' are chosen at $(0, 0, \pm 0.3)$ Å, which are the minima of the bare potential [44]. The free energy as a function of ΔE was computed by monitoring ΔE in a 2 ns, unconstrained MD run. The proton was treated quantum mechanically as well as classically. The results are shown in Fig. 6, where the heavy line is the quantum result and the thin line is the classical result. The barrier height for the quantum calculation is 4.35 kT and the minima are located at $\pm 2.98 \times 10^{-21}$ C/Å. For this choice of reaction coordinate, the free energy profiles are quadratic over much larger distance ranges about the potential minima and the barrier is sharper. The choice of reaction coordinate should not influence the computation of the full rate constant provided the barrier is sufficiently high to make transitions rare events. As we shall show in the next section, the solvent polarization is a convenient choice for the reaction coordinate in studies of the dynamics of proton transfer in condensed phases.

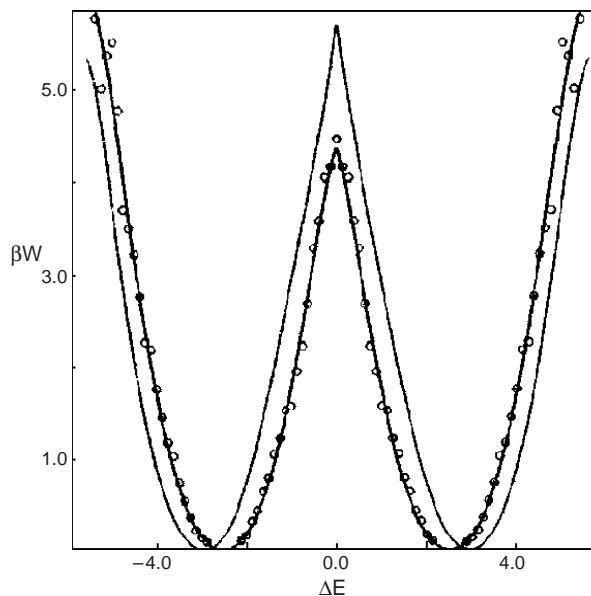


Figure 6. Free energy profiles using the solvent polarization as the reaction coordinate. The heavy and thin solid lines correspond to the least squares fitting of the unconstrained calculations for the quantum and classical protons, respectively. The open circles are the simulation results for the quantum proton. The units for ΔE are 10^{21} C/Å.

4. ADIABATIC REACTION DYNAMICS

Thus far, we have focused on the free energy along the reaction coordinate. In this section, we consider dynamics and the computation of the reaction rate constant. Instead of treating the most general situation of nonadiabatic dynamics, which is the topic of the next section, we begin with a study of the adiabatic dynamics of a quantum reactive system in bath or environment of classical particles. Adiabatic dynamics has been used to compute proton transfer rates [44, 49].

From a theoretical perspective, the treatment of adiabatic dynamics is conceptually simple; one needs to solve the Schrödinger equation for the relevant quantum degrees of freedom in the fixed field of the classical particles to determine the ground state energy as a function of the positions of the classical particles. The motions of the classical particles are, in turn, governed by Newton's equations of motion with Hellmann-Feynman forces derived from the ground state potential energy function. Here we outline how such a description follows from an approximation to the full quantum correlation function expression for the rate coefficient and present examples to illustrate adiabatic reaction dynamics.

4.1. Quantum-Classical Adiabatic Dynamics

We begin by sketching a derivation of the expression for the rate of a chemical reaction for quantum-classical adiabatic dynamics [6]. The starting point of the analysis is the quantum mechanical expression for the reaction rate given earlier [see Eq. (11)].

We suppose that the quantum system is described by the Hamiltonian

$$\hat{H} = \frac{\hat{P}^2}{2M} + \frac{\hat{p}^2}{2m} + \hat{V}(\hat{q}, \hat{Q}) \quad (36)$$

where \hat{q} and \hat{Q} are the coordinate operators of the quantum subsystem and bath, respectively, and the potential energy operator is $\hat{V}(\hat{q}, \hat{Q})$. Also, we denote the corresponding momentum operators and masses by lower and upper case letters, respectively. We shall consider the limit where the masses M of the bath particles are much larger than those of the quantum subsystem particles, $M \gg m$.

To begin, we rewrite the trace in the quantum expression for the rate kernel $K(t)$ in Eq. (11) in the $\{Q\}$ representation for the bath degrees of freedom and retain the abstract notation for the quantum subsystem degrees of freedom,

$$K(t) = \frac{-1}{i\hbar\beta} \langle \hat{\chi}; \hat{\chi} \rangle^{-1} \text{Tr}' \int dQ \langle Q | [\hat{\chi}, \hat{\chi}(t)] \hat{\rho}_e | Q \rangle \quad (37)$$

The prime on the trace indicates that only the subsystem degrees of freedom are traced over. Next, we introduce a partial Wigner representation [50] of the bath degrees of freedom. The partial Wigner transform of any operator \hat{A} is

$$\hat{A}_W(R, P) = \int dZ e^{-iP \cdot Z/\hbar} \left\langle R + \frac{Z}{2} | \hat{A} | R - \frac{Z}{2} \right\rangle \quad (38)$$

and the partial Wigner transform of the equilibrium density matrix is

$$(\hat{\rho}_e)_W(R, P) = (2\pi\hbar)^{-3N} \int dZ e^{iP \cdot Z/\hbar} \left\langle R - \frac{Z}{2} | \hat{\rho}_e | R + \frac{Z}{2} \right\rangle \quad (39)$$

These quantities are still operators in the subsystem degrees of freedom.

The evaluation of the rate kernel requires the computation of the matrix elements of triple operator products whose partial Wigner transform is [51]

$$\int dQ \langle Q | \hat{A} \hat{B} \hat{\rho}_e | Q \rangle = \int dR dP [\hat{A}_W(R, P) e^{\hbar\Lambda/2i} \hat{B}_W(R, P)] (\hat{\rho}_e)_W(R, P) \quad (40)$$

where

$$\Lambda = \overleftarrow{\nabla}_P \cdot \overrightarrow{\nabla}_R - \overleftarrow{\nabla}_R \cdot \overrightarrow{\nabla}_P \quad (41)$$

and the directions of the arrows on the gradient operators indicate the directions in which these operators should be applied. Using these results the rate kernel takes the form,

$$K(t) = \langle \hat{\chi}; \hat{\chi} \rangle^{-1} \frac{1}{-i\hbar\beta} \text{Tr}' \int dRdP [\hat{\chi}_W(R, P) e^{\hbar\Lambda/2i} \hat{\chi}_W(R, P, t) - \hat{\chi}_W(R, P, t) e^{\hbar\Lambda/2i} \hat{\chi}_W(R, P)] (\hat{\rho}_e)_W(R, P) \quad (42)$$

where $\hat{\chi}_W(R, P, t) \equiv \hat{\chi}_W(t)$ is the solution of the equation of motion

$$\frac{d\hat{\chi}_W(t)}{dt} = \frac{i}{\hbar} [\hat{H}_W e^{\hbar\Lambda/2i} \hat{\chi}_W(t) - \hat{\chi}_W(t) e^{\hbar\Lambda/2i} \hat{H}_W] \quad (43)$$

Here the partial Wigner representation of the Hamiltonian is

$$\hat{H}_W(R, P) = \frac{P^2}{2M} + \frac{\hat{p}^2}{2m} + \hat{V}_W(\hat{q}, R) \quad (44)$$

Next, we take the limit where the bath particles are massive compared to those of the quantum subsystem. It is convenient to introduce scaled variables such that the momenta of the heavy particles have the same order of magnitude as the momenta of the light particles. Consequently, we scale distances by the characteristic wavelength of the light particles, $\lambda_m = (\hbar^2/m\epsilon_0)^{1/2}$, time in units of $t_0 = \hbar/\epsilon_0$. Here ϵ_0 is an energy unit, typically $\epsilon_0 = \beta^{-1}$. In these units the light particle momenta are scaled by $p_m = m\lambda_m/t_0 = (m/\epsilon_0)^{1/2}$ and the heavy particle momenta by $P_M = (M\epsilon_0)^{1/2}$. In scaled units $\hbar\Lambda/(2i) \rightarrow \mu\Lambda/(2i)$, and we may expand the equation of motion in the small parameter $\mu = (m/M)^{1/2}$. Expanding to linear order in μ and then returning to unscaled units, the equation of motion, Eq. (43), becomes [6].

$$\frac{d\hat{\chi}_W(t)}{dt} = \frac{i}{\hbar} [\hat{H}_W, \hat{\chi}_W(t)] - \frac{1}{2} (\{\hat{H}_W, \hat{\chi}_W(t)\} - \{\hat{\chi}_W(t), \hat{H}_W\}) \quad (45)$$

This is a quantum-classical Liouville equation for a dynamical variable [6, 52]. Carrying out a similar μ expansion, the rate kernel, Eq. (42), takes the form,

$$K(t) = \frac{1}{\beta} \langle \hat{\chi}; \hat{\chi} \rangle^{-1} \text{Tr}' \int dRdP \left(\frac{i}{\hbar} [\hat{\chi}_W, \hat{\chi}_W(t)] - \frac{1}{2} (\{\hat{\chi}_W, \hat{\chi}_W(t)\} - \{\hat{\chi}_W(t), \hat{\chi}_W\}) \right) (\hat{\rho}_e)_W \quad (46)$$

We may evaluate this expression (45) in any convenient representation and for this purpose we choose the basis of adiabatic eigenstates of the Hamiltonian operator $\hat{h}_W(R) = \hat{p}^2/2m + \hat{V}_W(q, R)$:

$$\hat{h}_W(R)|\alpha; R\rangle = E_\alpha(R)|\alpha; R\rangle \quad (47)$$

Equation (46) can also be represented in this basis. This analysis is the starting point for a systematic approach to nonadiabatic dynamics which will be presented in some detail in the next section. Here we will be concerned solely with the adiabatic limit where the dynamics is assumed to take place on a single adiabatic surface. In this case, the adiabatic representation of Eq. (45) takes an especially simple form,

$$\frac{d\chi_W^\alpha(t)}{dt} = \{\chi_W^\alpha(t), H_W^\alpha\} \quad (48)$$

where $\chi_W^\alpha = \langle \alpha; R | \hat{\chi}_W(t) | \alpha; R \rangle$ and $H_W^\alpha = P^2/2M + E_\alpha(R)$. This is just a classical evolution equation but with Hellmann-Feynman forces,

$$F_W^\alpha = -\langle \alpha; R | \nabla \hat{h}_W(R) | \alpha; R \rangle = -\frac{\partial E_\alpha(R)}{\partial R} \quad (49)$$

determined by the potential $E_\alpha(R)$ obtained from the solution of the Schrödinger equation for the α adiabatic eigenstate. The rate kernel may be written in the adiabatic limit as

$$K^\alpha(t) = \langle \chi_W^\alpha \chi_W^\alpha \rangle^{-1} \frac{1}{\beta} \int dRdP \{\chi_W^\alpha(t), \chi_W^\alpha\} \rho_{We}^\alpha \quad (50)$$

with $\rho_{We}^\alpha(R, P) = e^{-\beta H_W^\alpha} / \int dR dP e^{-\beta H_W^\alpha}$. The algorithm for adiabatic mixed quantum-classical dynamics is simple. The dynamical variables depend on the classical coordinates (R, P) and the adiabatic state $|\alpha; R\rangle$. The classical coordinates evolve by Newton's equations of motion but with Hellmann-Feynman forces corresponding to the α adiabatic state determined as a function of the instantaneous position R .

4.2. Adiabatic Proton-Transfer Reactions in Solution

We now return to the study of proton transfer reactions in strongly hydrogen bonded complexes but now embedded in a bulk solvent of dipolar molecules with dipole moment 5.0 D. The molecular dynamics calculations we describe were carried out for a system of $N = 342$ solvent molecules, two ions, and a proton in a cubic box with periodic boundary conditions [44]. The simulations of the dynamics of the quantum proton coupled to the classical solvent were carried out as follows. Given a configuration of the solvent, the Schrödinger equation,

$$H(r; R)\Psi(r; R) = E(R)\Psi(r; R) \quad (51)$$

where $H(r; R)$ is the Hamiltonian for the proton with coordinate r in the fixed field of the classical particles with coordinates R , was solved by expanding the proton wave function in a set of $n = 156$ localized Gaussian functions $\phi_i(r)$ as

$$\Psi(r; R) = \sum_{i=1}^n c_i(R)\phi_i(r) \quad (52)$$

yielding a standard (nonorthogonal) eigenvalue problem from which the energies and eigenfunctions were obtained. After calculating the proton ground state wave function $\Psi_0(r; R)$ and energy $E_0(R)$, the proton contribution to the force acting on every site of the solvent was calculated. Given these forces, the solvent equations of motion,

$$M_i \ddot{R}_i = -\nabla_{R_i} E_0(R) \quad (53)$$

were integrated.

Solution of the eigenvalue problem in the absence of the solvent yields an energy spacing between the ground and first excited states which is somewhat greater than $k_B T$, just within the region of validity of the adiabatic approximation. In the presence of solvent, the energy gap is large when the proton is hydrogen bonded to one of the ions (reactant or product configurations) but is comparable to that in the absence of solvent when the proton is in the vicinity of the activated region. Proton transfer events are triggered by solvent fluctuations that provide no preferential solvation for either ion, making this an interesting reaction in which to study solvent effects on quantum reactive events.

The choice of the reaction coordinate depends on the nature of the transition process, and there are a number of possible ways to construct a function of the solvent coordinates that can be used to monitor the proton transfer. A possible choice of the reaction coordinate is the mean value of the z component of the position of the proton,

$$\xi(R) = \bar{z}(R) = \langle \Psi_0(R) | \hat{z} | \Psi_0(R) \rangle \quad (54)$$

If the reaction involves the passage of the proton from a region near one ion to the other, configurations with negative and positive values for ξ would correspond to reactant and product states, respectively. By symmetry, the activated state is located at $\xi = \xi^\ddagger = 0$.

The solvent polarization $\Delta E(R)$ [see Eq. (35)] is another, more convenient, choice for the reaction coordinate because it reflects the participation of the solvent in the proton transfer process. Furthermore, because $\Delta E(R)$ is an analytical function of the solvent coordinates, it is easy to generate trajectories in which the initial states are located at the transition state using blue moon sampling.

The expression (17) for the TST rate constant, specialized to the polarization reaction coordinate is

$$k^{TST} = (2\pi\beta)^{1/2} \frac{\langle D^{1/2} \delta(\Delta E - \Delta E^\ddagger) \rangle}{\langle \theta(\Delta E - \Delta E^\ddagger) \rangle} \quad (55)$$

where

$$D = \frac{1}{2m} \sum_i \left(\sum_{\alpha} \nabla_{i,\alpha} \Delta E \right)^2 \quad (56)$$

assuming all solvent masses are equal. The reaction coordinate ΔE and its time derivative are not statistically independent, and the expected value in the expression for k^{TST} does not factor into coordinate and velocity contributions [17].

Equation (55) can be calculated in the blue moon ensemble as discussed earlier [see Eq. (18)] using the expression,

$$k^{TST} = (2\pi\beta)^{-1/2} \frac{\langle \delta(\Delta E - \Delta E^{\ddagger}) \rangle}{\langle D^{-1/2} \rangle_{\Delta E=0} \langle \theta(\Delta E - \Delta E^{\ddagger}) \rangle} \quad (57)$$

Using this formula, the TST value for the rate coefficient was found to be $k^{TST} = (4.03 \pm 0.29) \times 10^9 \text{ s}^{-1}$ [44].

Deviations from transition-state theory are accounted for by the transmission coefficient $\kappa = \kappa(t^*)$, where $\tau_{mic} \ll t^* \ll \tau_p$, with τ_{mic} a time that characterizes the relaxation of the microscopic degrees of freedom and τ_p the proton transfer time. The transmission coefficient takes the form,

$$\kappa(t) = \frac{\langle D^{-1/2} \dot{\Delta E} \theta[\Delta E(t)] \rangle_{\Delta E=0}}{\langle D^{-1/2} \dot{\Delta E} \theta(\Delta E) \rangle_{\Delta E=0}} \quad (58)$$

Figure 7 shows the time-dependent transmission coefficient. Initial state configurations were generated using the blue moon ensemble. At $t = 0$, the constraint on the reaction coordinate was released, and particle velocities were assigned according to the generalization of Boltzmann statistics for rigid diatomic molecules. From these simulations, the transmission coefficient is estimated to be $\kappa = 0.57 \pm 0.11$. There is a non-negligible deviation from TST for this proton transfer process.

4.3. Proton Transfer Dynamics in Nanoclusters

We next consider the same proton-ion complex but now embedded in a mesoscopic molecular cluster [53] instead of a bulk condensed phase. Again we treat the proton dynamics adiabatically. Calculations were performed for clusters of $N = 20$ and $N = 67$ solvent molecules at temperatures of 200 and 260 K, respectively. Under these conditions, the clusters were in the liquid state. Evaporation did not occur on the timescale of the simulations, typically several nanoseconds. As discussed earlier, both the average proton position and the solvent polarization can be used to track the hops of the proton between the reactant and product configurations.

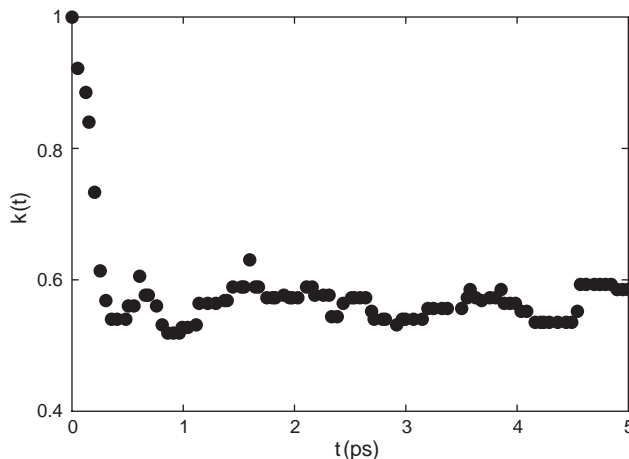


Figure 7. The time-dependent transmission coefficient for adiabatic dynamics.

The cluster solvent molecules tended to strongly solvate the part of the proton-ion complex with the more exposed negative charge; that is, the end of the complex that is less strongly bonded to the H^+ ion. This suggests that the complex tends to “float” on the surface of the cluster. When the H^+ ion is strongly bound to one A^- ion, this $A-H$ dipole has a smaller dipole moment than that of a solvent molecule. Consequently, the solvent-solvent interactions are stronger than the interactions between a solvent molecule and this part of the proton-ion complex. These energetic arguments suggest that it may be favorable for this end of the proton-ion complex to reside on the surface of the cluster, a fact supported by the simulation results. Of course, both entropic as well as energetic factors come into play in determining the structure of mixed clusters [54] but, in the cases studied, energetic factors played a dominant role.

The position of the proton-ion complex in the cluster has a strong influence on the nature of the proton transfer dynamics. In the case of a 20 molecule cluster the complex resides for long portions of time on the surface of the cluster and long portions of time in the interior of the cluster. If the complex is on the surface of the cluster, then transitions rarely occur; however, if the complex makes an excursion into the interior, then this excursion correlates with a proton transfer. The picture is somewhat different for the 67 molecule cluster. The proton-ion complex rarely penetrates deeply into the cluster. Some of the proton transfer events correlate with excursions of the complex into the cluster, but only one solvent layer deep and never far from the surface. However, even when the complex floats on the surface of the cluster, there are frequent proton transfer events. Figure 8 shows such a proton transfer event. Initially, the proton (gray) is strongly bound to the one of the ions (black) in the complex. The complex resides on the surface of the cluster with one end, to which the proton is weakly bound, solvated in the cluster, and the other end extending out of the cluster. In the course of time, a fluctuation occurs that causes the complex to assume a configuration parallel to the surface so that there is a more nearly equal solvation of the two ends of the complex. This is a favorable configuration for the proton transfer so that it takes place in frame (a) of this figure. Once the proton transfer is complete, then the favorable complex configuration is for the now strongly hydrogen bonded end to protrude from the cluster and the weakly bound end to lie within the cluster [frame (b)].

Thus, the mechanism of the proton transfer depends on the size of the cluster. For smaller clusters, fluctuations lead to penetration of the complex into the interior of the cluster where proton transfer is likely. For larger clusters, transitions occur primarily by orientational motion of the complex on the surface of the cluster or when the complex makes shallow penetrations into the cluster. Deep penetrations of the complex into the cluster are rare. For the smaller 20 molecule cluster, presumably the orientational motion of the complex is restricted on the surface due to the larger surface forces.

Figure 9 shows the transmission coefficient as a function of time for the 67 molecule cluster. The results in this figure show a rapid decay on a timescale that is less than a picosecond followed by a somewhat longer decay, of the order of a few picoseconds, to a plateau value. From this graph, the transmission coefficient may be determined from the plateau values and one finds $\kappa = 0.4$. The timescale for the establishment of a plateau in $\kappa(t)$ is longer in the

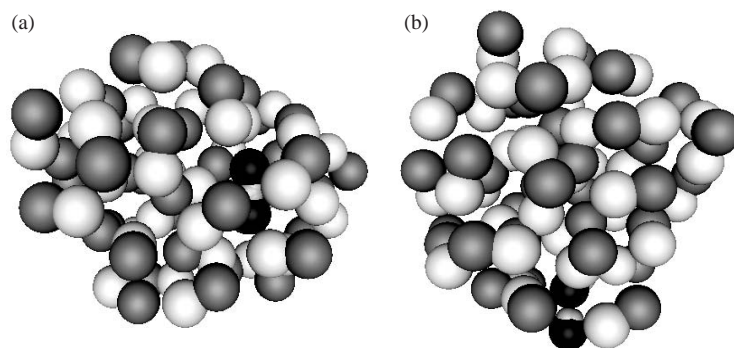


Figure 8. Cluster configurations during (a) and after (b) a proton transfer event for a 67 molecule cluster.

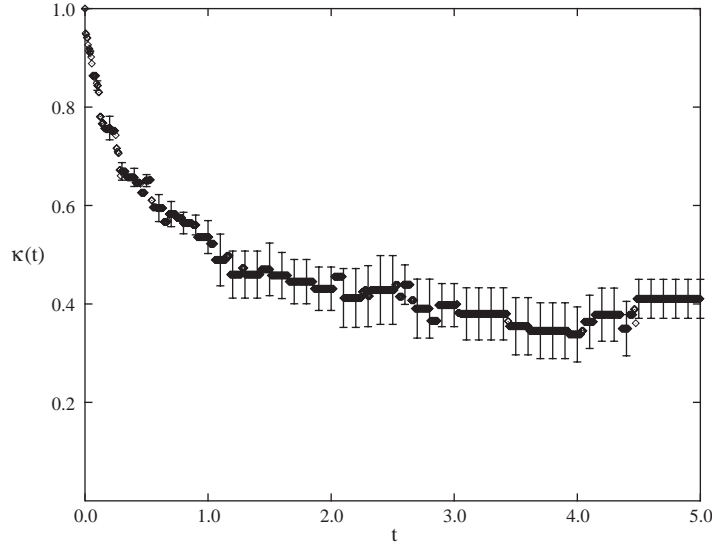


Figure 9. Transmission coefficient as a function of time for a 67 solvent molecule cluster.

cluster environment than in the bulk for a similar but not identical intrinsic potential. This again signals different dynamics in the cluster compared to the bulk.

5. MEAN FIELD AND SURFACE HOPPING DYNAMICS

There are many instances where the dynamics can take place on more than one potential energy surface and transitions between different quantum states must be taken into account. In such cases, the adiabatic approximation is inadequate. Charge transfer in molecules is one example; nonradiative relaxation in molecular or condensed phase systems and the field of photochemistry provide other good examples.

In order to see how nonadiabatic effects enter the dynamics, we consider the total Hamiltonian for a system composed of light (mass m) particles with coordinates r and heavy (mass M) particles with coordinates R ,

$$H(r, R) = -\frac{\hbar^2}{2M} \frac{\partial^2}{\partial R^2} + h(r; R) \quad (59)$$

where $h(r; R) = -\frac{\hbar^2}{2m} \frac{\partial^2}{\partial r^2} + V(r, R)$ is the Hamiltonian for the light particles in the field of the fixed heavy particles. The adiabatic basis is given by the solution of the eigenvalue problem $\hat{h}|\alpha; R\rangle = E_\alpha(R)|\alpha; R\rangle$. We let $\langle r|\alpha; R\rangle = \phi_\alpha(r; R)$ be the adiabatic wave function for state α and make the ansatz

$$\Psi(r, R, t) = \sum_{\alpha} \psi_{\alpha}(R, t) \phi_{\alpha}(r; R) \quad (60)$$

for the wave function of the entire system. Substitution into the time-dependent Schrödinger equation

$$i\hbar \frac{\partial}{\partial t} \Psi(r, R, t) = H \Psi(r, R, t) \quad (61)$$

yields the following equation for the wave function for the heavy mass degrees of freedom:

$$i\hbar \frac{\partial}{\partial t} \psi_{\alpha}(R, t) = \left[-\frac{\hbar^2}{2M} \frac{\partial^2}{\partial R^2} + E_{\alpha}(R) \right] \psi_{\alpha}(R, t) + \sum_{\alpha'} C_{\alpha\beta} \psi_{\alpha'}(R, t) \quad (62)$$

where we have introduced the coupling operator

$$C_{\alpha\alpha'} = \left\langle \alpha; R \left| \frac{\hat{P}^2}{2M} \right| \alpha'; R \right\rangle - \frac{\hbar^2}{M} \langle \alpha; R | \nabla_R | \alpha'; R \rangle \cdot \nabla_R \quad (63)$$

where $\hat{P}^2/2M$ is the kinetic energy operator. The diagonal elements $C_{\alpha\alpha}$ give corrections to the adiabatic eigenvalues E_α , and the off-diagonal terms describe the coupling between the different quantum states. When $C_{\alpha\beta} \approx 0$ (Born-Oppenheimer approximation), we recover adiabatic dynamics.

We next consider various schemes for constructing mixed quantum-classical dynamics that allow for nonadiabatic effects. The quantum and classical degrees of freedom interact and their dynamics must be treated in a consistent fashion. Time-dependent variations of the classical degrees of freedom induce transitions between quantum states of the light mass subsystem and these transitions, in turn, modify the forces that govern the motion of the classical particles. Ehrenfest (or mean-field) and surface-hopping schemes are two approximate mixed quantum-classical methods to describe nonadiabatic dynamics [55]. Quantum-classical Liouville dynamics provides a more rigorous approach to nonadiabatic dynamics.

5.1. Mean-Field Method

The mean field approach is based on Ehrenfest's equations of motion for the evolution of the position and momentum operators of the heavy mass particles. Assuming that the expectation value of a function can be approximated by the function of the expectation value, we obtain the following mean field equations,

$$\begin{aligned}\frac{dR(t)}{dt} &= \frac{P(t)}{M} \\ \frac{dP(t)}{dt} &= -\nabla \langle \psi[R(t), t] | \hat{h}[R(t)] | \psi[R(t), t] \rangle\end{aligned}\quad (64)$$

where the wave function evolves through the time-dependent Schrödinger equation,

$$i\hbar \frac{\partial}{\partial t} |\psi[R(t), t]\rangle = \hat{h}[R(t)] |\psi[R(t), t]\rangle \quad (65)$$

According to these equations, the heavy mass degrees of freedom evolve classically along a single *mean* trajectory determined by the effective potential energy surface $E_{ef}[R(t)] = \langle \psi[R(t), t] | \hat{h}[R(t)] | \psi[R(t), t] \rangle$. Mean-field methods have been used to compute proton transfer rates. [56, 57] Outside strong interaction regions, the quantum system will typically collapse onto a given state, and the mean field equations will likely be a poor approximation to the dynamics. Surface-hopping algorithms have been devised to account for this difficulty.

5.2. Surface-Hopping Dynamics

In surface-hopping dynamics, the system evolves on specified adiabatic energy surfaces interspersed by quantum transitions that occur probabilistically and change the state of the system. Observables are computed from an average over an ensemble of such surface-hopping trajectories. A variety of such schemes have been proposed. One of the most popular is Tully's fewest switches algorithm [55, 58]. In this method, the time-dependent Schrödinger equation (65) is solved by expanding the wave function in the instantaneous adiabatic eigenstates of the Hamiltonian $\hat{h}[R(t)]$, $\hat{h}[R(t)]|\alpha; R(t)\rangle = E_\alpha[R(t)]|\alpha; R(t)\rangle$,

$$|\Psi(R(t), t)\rangle = \sum_{\alpha} c_{\alpha}(t) |\alpha; R(t)\rangle \quad (66)$$

yielding the evolution equation for the coefficients

$$i\hbar \frac{dC_{\alpha}(t)}{dt} = (E_{\alpha} - E_0)C_{\alpha}(t) - i\hbar \sum_{\alpha'} \frac{P}{M} \cdot d_{\alpha\alpha'} C_{\alpha'}(t) \quad (67)$$

where $d_{\alpha\alpha'} = \langle \alpha; R(t) | \nabla_{R(t)} | \alpha'; R(t) \rangle$ is the nonadiabatic coupling matrix element and

$$C_{\alpha}(t) = c_{\alpha}(t) \exp \left\{ i \int_0^t dt' E_0[R(t')] / \hbar \right\} \quad (68)$$

During each molecular dynamics time step Δ , the classical degrees of freedom evolve by Newton's equation of motion subject to Hellmann-Feynman forces that depend on

instantaneous adiabatic eigenstates. The probability of a hop from state α to α' is given by

$$w_{\alpha\alpha'} = \gamma_{\alpha\alpha'} \theta(\gamma_{\alpha\alpha'}) \quad (69)$$

where $\theta(x)$ is the Heaviside function and

$$\gamma_{\alpha\alpha'} = \frac{-2\Re\{\rho_{\alpha'\alpha}^*(t+\Delta)[P(t)/M] \cdot d_{\alpha\alpha'}[R(t)]\Delta\}}{\rho_{\alpha\alpha}(t+\Delta)} \quad (70)$$

Here $\rho^{\alpha\alpha'}(t)$ is a matrix element of the density matrix in the adiabatic basis, $\rho^{\alpha\alpha'}(t) = \langle \alpha; R(t) | \hat{\rho}(t) | \alpha'; R(t) \rangle = \langle \alpha; R(t) | \Psi[R(t), t] \rangle \langle \Psi[R(t), t] | \alpha'; R(t) \rangle = c_{\alpha'}^*(t) c_{\alpha}(t)$.

Pechukas [59] presented a description of nonadiabatic dynamics based on an analysis of the Feynman path integral expression for the propagator. The equations of motion for the bath degrees of freedom involve a nonlocal quantum force. Surface-hopping schemes that use approximations to this nonlocal force have been constructed by Rossky et al. [60] and Coker et al. [61]. In particular, Coker and Xiao [61] have shown that a short time approximation that localizes the Pechukas force leads to Tully's algorithm.

5.3. Nonadiabatic Proton Transfer in Nanoclusters

Surface-hopping schemes have been used to study proton and hydrogen atom transfer rates in the condensed phase [62] and in biosystems [63]. We begin with an investigation of nonadiabatic effects on proton transfer rates in nanoclusters using Tully's surface-hopping dynamics [53].

The model system is the same as that described in Section 4.3, namely, a proton-ion complex embedded in a cluster of polar diatomic molecules. The average position of the proton $\bar{z}(R) = \langle \alpha; R(t) | \hat{z} | \alpha; R(t) \rangle$ is shown in Fig. 10 (bottom panel) as a function of time for a nonadiabatic reactive trajectory. The upper panel of the figure shows the protonic

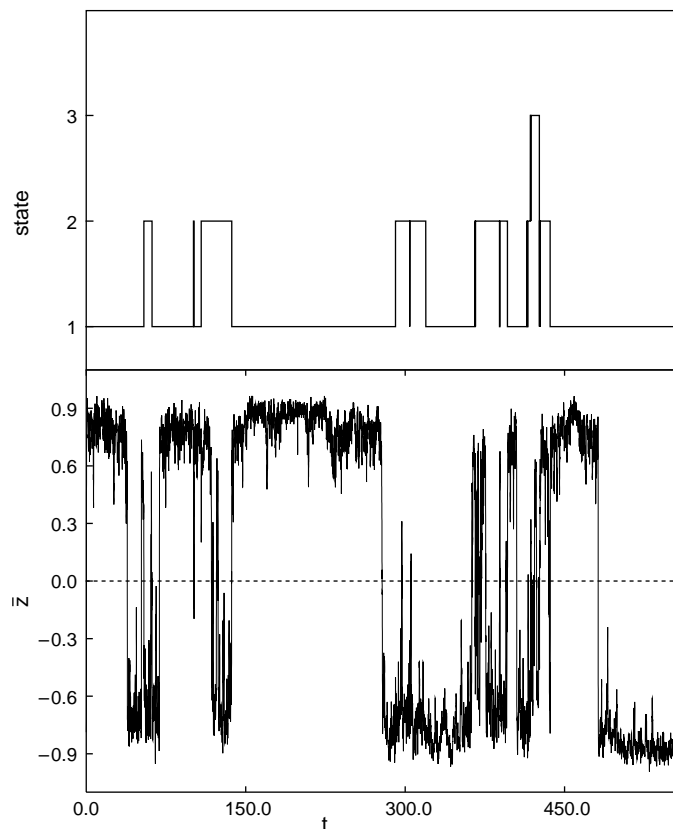


Figure 10. (top) Protonic state, (bottom) expectation value of the position of the proton \bar{z} as a function of time for a 67-molecule cluster.

state determined by the stochastic algorithm that is used to compute the Hellmann-Feynman forces for the classical particles. Nonadiabatic transitions frequently occur when the proton transfers to and from reactant and product configurations. This breakdown of the adiabatic approximation occurs because the transition state configurations correspond to a nearly symmetrical solvation of the proton-ion complex, and the energy gap between the lowest adiabatic states is small for such configurations. The three lowest adiabatic energies for a short time interval close to the transition state regime are shown in Fig. 11. The black dots denote the path of the proton in the proton state space. The three lowest eigenvalues show similar time variations. Proton hops between the different states occur by jump transitions when the difference between the energy states is close to 1–2 kT.

Nonadiabatic transitions influence the mechanism and rate of the reaction. When the proton is in an excited state, the proton density is diffuse and symmetric, and solvent configurations that favor the transition state are favored. As a result, the number of quantum transitions and proton recrossing attempts increase. This changes the transfer rate. The rate constant for the reaction was computed by counting the number of proton transfers in the nonadiabatic dynamics trajectories and was found to be $\kappa = 0.011 \text{ ps}^{-1}$. The dynamics is dominated by the ground state, and the change in the rate due to surface hopping is not great for this model system. In systems where the nonadiabatic character is more pronounced, effects due to proton hops to the excited states will have important implications for the mechanisms and rates of the reaction.

6. QUANTUM-CLASSICAL LIOUVILLE EQUATION

Both mean-field and surface-hopping dynamics make assumptions about the nature of the time evolution of the system. Mean-field equations assume that the Hellmann-Feynman forces that govern the classical degrees of freedom can be computed from the time-evolving wave function. Surface-hopping dynamics assumes that the classical degrees of freedom evolve on adiabatic potential energy surfaces with quantum transitions determining switches among different potential surfaces. We now show how quantum-classical dynamics can be derived from quantum Liouville equation by carrying out an expansion of the evolution operator in the small parameter $\mu = (m/M)^{1/2}$ introduced in Section 4.1 [52]. We again consider a quantum system with Hamiltonian given by Eq. (36) whose time evolution is described by the quantum Liouville or von Neumann equation,

$$\frac{\partial \hat{\rho}}{\partial t} = -\frac{i}{\hbar} [\hat{H}, \hat{\rho}] \quad (71)$$

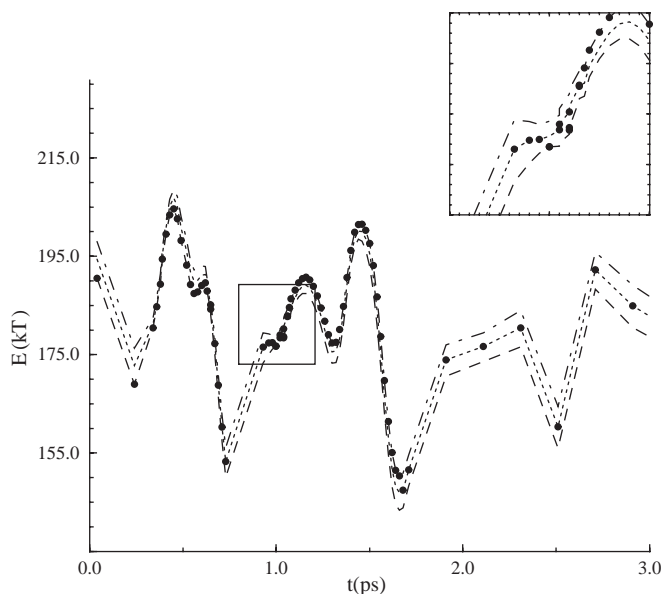


Figure 11. Instantaneous protonic adiabatic eigenstates as a function of time.

If we take the partial Wigner transform [defined in Eqs. (38) and (39)] of this equation we obtain,

$$\begin{aligned} \frac{\partial \hat{\rho}_W(R, P, t)}{\partial t} &= -\frac{i}{\hbar} \left[(\hat{H} \hat{\rho})_W - (\hat{\rho} \hat{H})_W \right] \\ &= -\frac{i}{\hbar} \left[\hat{H}_W(R, P) e^{\hbar \Lambda / 2i} \hat{\rho}_W(R, P, t) - \hat{\rho}_W(R, P, t) e^{\hbar \Lambda / 2i} \hat{H}_W(R, P) \right] \end{aligned} \quad (72)$$

which is the analog of Eq. (45) for a dynamical variable. The operator Λ is defined in Eq. (41) and is the negative of the Poisson bracket operator. Scaling variables as discussed earlier for adiabatic dynamics, expanding in μ and finally returning to unscaled variables we obtain the quantum-classical Liouville equation [52, 64–68],

$$\begin{aligned} \frac{\partial \hat{\rho}_W(R, P, t)}{\partial t} &= -\frac{i}{\hbar} [\hat{H}_W(R, P), \hat{\rho}_W(R, P, t)] \\ &\quad + \frac{1}{2} \left(\left\{ \hat{H}_W(R, P), \hat{\rho}_W(R, P, t) \right\} - \left\{ \hat{\rho}_W(R, P, t), \hat{H}_W(R, P) \right\} \right) \\ &\equiv -i \hat{\mathcal{L}} \hat{\rho}_W(R, P, t) = -[\hat{H}_W, \hat{\rho}_W(R, P, t)] \end{aligned} \quad (73)$$

where the last line defines the quantum-classical Liouville operator, \mathcal{L} , and the quantum-classical bracket, (\cdot, \cdot) [69, 70].

To construct a surface-hopping picture of the dynamics we consider the representation of this equation in a basis of adiabatic eigenstates defined in Eq. (47). Taking matrix elements of Eq. (73) and letting $\rho_W^{\alpha\alpha'}(R, P) = \langle \alpha; R | \hat{\rho}_W(R, P) | \alpha'; R \rangle$, we obtain

$$\frac{\partial \rho_W^{\alpha\alpha'}(R, P, t)}{\partial t} = \sum_{\beta\beta'} -i \mathcal{L}_{\alpha\alpha', \beta\beta'} \rho_W^{\beta\beta'}(R, P, t) \quad (74)$$

where

$$-i \mathcal{L}_{\alpha\alpha', \beta\beta'} = (-i \omega_{\alpha\alpha'} - i L_{\alpha\alpha'}) \delta_{\alpha\beta} \delta_{\alpha'\beta'} + J_{\alpha\alpha', \beta\beta'} \equiv -i \mathcal{L}_{\alpha\alpha'}^0 + J_{\alpha\alpha', \beta\beta'} \quad (75)$$

where $\omega_{\alpha\alpha'}(R) = [E_\alpha(R) - E_{\alpha'}(R)]/\hbar = \Delta E_{\alpha\alpha'}/\hbar$ and J is defined by

$$J_{\alpha\alpha', \beta\beta'} = -\frac{P}{M} \cdot d_{\alpha\beta} \left(1 + \frac{1}{2} S_{\alpha\beta} \cdot \frac{\partial}{\partial P} \right) \delta_{\alpha'\beta'} - \frac{P}{M} \cdot d_{\alpha'\beta'}^* \left(1 + \frac{1}{2} S_{\alpha'\beta'}^* \cdot \frac{\partial}{\partial P} \right) \delta_{\alpha\beta} \quad (76)$$

and the nonadiabatic coupling matrix element is $d_{\alpha\alpha'} = \langle \alpha; R | \partial / \partial R | \alpha'; R_0 \rangle$, and

$$S_{\alpha\beta} = \Delta E_{\alpha\alpha'} d_{\alpha\beta} \left(\frac{P}{M} \cdot d_{\alpha\beta} \right)^{-1} \quad (77)$$

The classical Liouville operator involving the mean of the Hellmann-Feynman forces for states α and α' is

$$i L_{\alpha\alpha'} = \frac{P}{M} \cdot \frac{\partial}{\partial R} + \frac{1}{2} (F_W^\alpha + F_W^{\alpha'}) \cdot \frac{\partial}{\partial P} \quad (78)$$

The quantum-classical Liouville equation may be integrated and solved by iteration to yield a representation of the dynamics as a sequence of terms involving increasing numbers of nonadiabatic transitions [52],

$$\begin{aligned} \rho_W^{\alpha_0\alpha'_0}(R, P, t) &= e^{-i \mathcal{L}_{\alpha_0\alpha'_0}^0 t} \rho_W^{\alpha_0\alpha'_0}(R, P) + \sum_{n=1}^{\infty} \sum_{(\alpha_1\alpha'_1)\dots(\alpha_n\alpha'_n)} \int_0^{t_0} dt_1 \int_0^{t_1} dt_2 \dots \int_0^{t_{n-1}} dt_n \\ &\quad \times \prod_{k=1}^n \left[e^{-i \mathcal{L}_{\alpha_{k-1}\alpha'_{k-1}}^0 (t_{k-1}-t_k)} J_{\alpha_{k-1}\alpha'_{k-1}, \alpha_k\alpha'_k} \right] e^{-i \mathcal{L}_{\alpha_n\alpha'_n}^0 t_n} \rho_W^{\alpha_n\alpha'_n}(R, P) \end{aligned} \quad (79)$$

Here $\rho_W^{\alpha\alpha'}(R, P)$ is the initial value of the density matrix element. In this equation, the diagonal part of the quantum-classical evolution operator, $\exp\{i\mathcal{L}_{\alpha\alpha'}^0 t\}$, may be written in terms of classical evolution on the $(\alpha\alpha')$ surface and a phase factor as,

$$\begin{aligned} e^{-i\mathcal{L}_{\alpha\alpha'}^0(t-t')} &= e^{-i\int_{t'}^t d\tau \omega_{\alpha\alpha'}(R_{\alpha\alpha'}, \tau)} e^{-iL_{\alpha\alpha'}(t-t')} \\ &\equiv W_{\alpha\alpha'}(t, t') e^{-iL_{\alpha\alpha'}(t-t')} \end{aligned} \quad (80)$$

The successive terms in the series correspond to increasing numbers of nonadiabatic transitions, starting with the first term that describes simple adiabatic dynamics. As an example, consider the calculation of the diagonal element of the density matrix, $\rho_W^{\alpha\alpha}(R, P, t)$. The contributions to this matrix element are determined by backward evolution from time t to time 0. The first term in the series corresponds to adiabatic evolution on state α . The next term accounts for single nonadiabatic transitions to states β ($\beta \neq \alpha$), which occur at times t' intermediate between t and 0. These transitions are accompanied by continuous momentum changes in the environment specified by the term in J involving a momentum derivative. Because a single quantum transition takes place, this contribution must come from an off-diagonal density matrix element, $\rho_W^{\alpha\beta}$ at time 0. During the portion of the evolution segment from t' to 0, the classical bath phase space coordinates are propagated on the mean of the two α and β adiabatic surfaces and a phase factor $W_{\alpha\beta}$ contributes to the population in state α .

The terms involving the bath momentum derivative in J are difficult to evaluate exactly. Consequently, we make a ‘‘momentum-jump’’ approximation that gives J the structure of a momentum translation operator whose effect on any function of the momentum is to shift the momentum by some value [52, 70]. To derive this approximation, we first consider the operator identity, $(S_{\alpha\beta}/2) \cdot \frac{\partial}{\partial P} = \Delta E_{\alpha\beta} M \frac{\partial}{\partial(P \cdot \hat{d}_{\alpha\beta})^2}$. The action of the operator on any function $f(P)$ of the momentum may be written approximately as

$$\begin{aligned} \left[1 + \Delta E_{\alpha\beta} M \frac{\partial}{\partial(P \cdot \hat{d}_{\alpha\beta})^2} \right] f(P) &\approx e^{\Delta E_{\alpha\beta} M \partial / \partial (P \cdot \hat{d}_{\alpha\beta})^2} f(P) \\ &= f \left[\hat{d}_{\alpha\beta}^\perp (P \cdot \hat{d}_{\alpha\beta}^\perp) + \hat{d}_{\alpha\beta} \text{sgn}(P \cdot \hat{d}_{\alpha\beta}) \sqrt{(P \cdot \hat{d}_{\alpha\beta})^2 + \Delta E_{\alpha\beta} M} \right] \\ &= f(P + \hat{d}_{\alpha\beta} \Delta P) \end{aligned} \quad (81)$$

where $\Delta P = -(\hat{d}_{\alpha\beta} \cdot P) + \text{sgn}(P \cdot \hat{d}_{\alpha\beta}) \sqrt{(P \cdot \hat{d}_{\alpha\beta})^2 + \Delta E_{\alpha\beta} M}$. In the second approximate equality on the right-hand side of this equation, we have replaced the sum by an exponential. The momentum vector may be written in terms of its components along $\hat{d}_{\alpha\beta}$ and a perpendicular vector $\hat{d}_{\alpha\beta}^\perp$, $P = \hat{d}_{\alpha\beta} (\hat{d}_{\alpha\beta} \cdot P) + \hat{d}_{\alpha\beta}^\perp (\hat{d}_{\alpha\beta}^\perp \cdot P)$. In the last line, we used the fact that the exponential operator is a translation operator in the variable $(P \cdot \hat{d}_{\alpha\beta})^2$. Using this momentum jump approximation, a member of the ensemble of trajectories that is used to compute the density matrix elements is shown schematically in Fig. 12.

A similar set of equations with similar interpretations can be written for an operator $\hat{A}_W(R, P)$. We have,

$$\begin{aligned} A_W^{\alpha_0\alpha'_0}(R, P, t) &= e^{i\mathcal{L}_{\alpha_0\alpha'_0}^0 t} A_W^{\alpha_0\alpha'_0}(R, P) + \sum_{n=1}^{\infty} (-1)^n \sum_{(\alpha_1\alpha'_1)\dots(\alpha_n\alpha'_n)} \int_0^t dt_1 \int_{t_1}^t dt_2 \cdots \int_{t_{n-1}}^t dt_n \\ &\quad \times \prod_{k=1}^n \left[e^{i\mathcal{L}_{\alpha_{k-1}\alpha'_{k-1}}^0 (t_k - t_{k-1})} J_{\alpha_{k-1}\alpha'_{k-1}, \alpha_k\alpha'_k} \right] e^{i\mathcal{L}_{\alpha_n\alpha'_n}^0 (t - t_n)} A_W^{\alpha_n\alpha'_n}(R, P) \end{aligned} \quad (82)$$

In order to compute correlation functions, we require the quantum-classical time evolution of operators as we shall see when we consider the calculation of rate constants using this formalism.

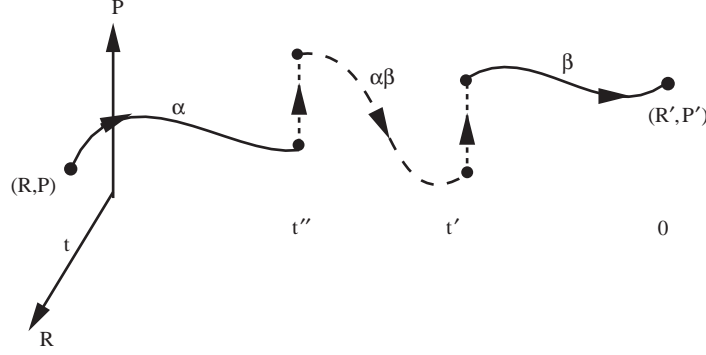


Figure 12. A trajectory segment with two nonadiabatic transitions that contributes to the diagonal element $\rho_W^{\alpha\alpha}(R, P, t)$ coming from $\rho_W^{\beta\beta}(R, P, t = 0)$. In the time segment between t'' and t' , the system evolves coherently and contains the phase factor $W_{\alpha\beta}$.

6.1. Simulation Algorithm

As we shall see below, in order to evaluate the time-dependent rate coefficient, the quantum-classical time evolution of the matrix elements of species operators must be computed. This evolution may be simulated using the sequential short-time algorithm [71, 72]. When the quantum-classical Liouville operator is time-independent, the evolution equation for the matrix elements of an operator or dynamical variable may be written as

$$\frac{d}{dt} A_W^{\alpha\alpha'}(R, P, t) = \sum_{\beta\beta'} i\mathcal{L}_{\alpha\alpha', \beta\beta'} A_W^{\beta\beta'}(R, P, t) \quad (83)$$

whose formal solution is

$$A_W^{\alpha\alpha'}(R, P, t) = \sum_{\beta\beta'} (e^{i\mathcal{L}t})_{\alpha\alpha', \beta\beta'} A_W^{\beta\beta'}(R, P, t) \quad (84)$$

Consequently, to compute the evolution we must be able to simulate the action of the quantum-classical propagator.

The propagator can be written simply as a composition of propagators in time segments of arbitrary length. For example, divide the time interval t into N segments of lengths $\Delta t_j = t_j - t_{j-1}$ so that

$$(e^{i\mathcal{L}t})_{\alpha_0\alpha'_0, \alpha_N\alpha'_N} = \sum_{(\alpha_1\alpha'_1), \dots, (\alpha_{N-1}\alpha'_{N-1})} \prod_{j=1}^N (e^{i\mathcal{L}(t_j - t_{j-1})})_{\alpha_{j-1}\alpha'_{j-1}, \alpha_j\alpha'_j} \quad (85)$$

In any of these time intervals, the propagator satisfies the Dyson equation, starting from

$$(e^{-i\mathcal{L}t})_{\alpha\alpha', \beta\beta'} = e^{-i\mathcal{L}^0_{\alpha\alpha'}t} \delta_{\alpha\beta} \delta_{\alpha'\beta'} + \sum_{\nu\nu'} \int_0^t dt' e^{-i\mathcal{L}^0_{\alpha\alpha'}(t-t')} J_{\alpha\alpha', \nu\nu'}(e^{-i\mathcal{L}t'})_{\nu\nu', \beta\beta'} \quad (86)$$

If Δt is sufficiently small, one can make a one-point approximation to the time integral in Eq. (86) by choosing a point t' in Δt . Letting $t' = t_j$, one obtains

$$\begin{aligned} (e^{i\mathcal{L}(t_j - t_{j-1})})_{\alpha_{j-1}\alpha'_{j-1}, \alpha_j\alpha'_j} &\approx e^{i\mathcal{L}^0_{\alpha_{j-1}\alpha'_{j-1}}(t_j - t_{j-1})} (\delta_{\alpha_{j-1}\alpha_j} \delta_{\alpha'_{j-1}\alpha'_j} - \Delta t J_{\alpha_{j-1}\alpha'_{j-1}, \alpha_j\alpha'_j}) \\ &= W_{\alpha_{j-1}\alpha'_{j-1}}(t_{j-1}, t_j) e^{iL_{\alpha_{j-1}\alpha'_{j-1}}(t_j - t_{j-1})} (\delta_{\alpha_{j-1}\alpha_j} \delta_{\alpha'_{j-1}\alpha'_j} - \Delta t J_{\alpha_{j-1}\alpha'_{j-1}, \alpha_j\alpha'_j}) \end{aligned} \quad (87)$$

At the end of each segment, the system may either stay on the same energy surface or make a transition to a new state.

The sequential short-time algorithm is easily implemented. The total time of the calculation is divided into a fixed number of time slices, the most natural choice being to take the molecular dynamics integration time step Δt as the length of the slice. The phase space

coordinates are propagated adiabatically in a time step, and the phase factor W is computed if the evolution is on the mean of two adiabatic surfaces. At the end of each time step, the probabilities $\Pi = |(P/M) \cdot d|\Delta t (1 + |(P/M) \cdot d|\Delta t)^{-1}$ and $\Sigma = 1 - \Pi$ are respectively used for acceptance or rejection of a quantum transition.

7. NONADIABATIC REACTION DYNAMICS

In this section we sketch a general formulation of the statistical mechanics of nonadiabatic chemical rate processes and give reactive flux correlation function expressions for the rate constant. We then illustrate the formalism with calculations on a two-level model system that captures the essential features of many transfer rate processes.

7.1. Quantum-Classical Reactive Flux Correlation Functions

The reactive-flux correlation functions that may be used to determine the rate constant for activated quantum processes can be derived using linear response theory [73]. We consider a multicomponent system where r independent chemical reactions take place. We may associate progress variables, $\bar{\chi}_i$, and affinities \mathcal{A}_i , ($i = 1, \dots, r$), with each independent reaction step. From linear irreversible thermodynamics, the chemical rate law describing the time evolution of the reaction rates \mathcal{J}_i takes the form [74],

$$\mathcal{J}_i \equiv \frac{d\bar{\chi}_i}{dt} = - \sum_{j=1}^r L_{ij} \beta \mathcal{A}_j \quad (88)$$

where L_{ij} is an Onsager coefficient.

To derive this rate law using linear response theory, we suppose the system is subject to external time-dependent forces (affinities) that couple to microscopic species variables $\hat{\chi}_{wi}$. The time-dependent Hamiltonian in the presence of the external forces is

$$\hat{\mathcal{H}}_W(t) = \hat{H}_W - \sum_{i=1}^r \hat{\chi}_{wi}^\dagger \mathcal{A}_i(t) \quad (89)$$

where the dagger stands for the adjoint. The species variables are in general operators in Hilbert space and functions of the classical phase space variables, $\hat{\chi}_{wi}(R, P)$.

The chemical rate law can be derived by calculating the nonequilibrium average of $\hat{\chi}_{wi}$,

$$\mathcal{J}_i \equiv \frac{d\overline{\hat{\chi}_{wi}}(t)}{dt} = \text{Tr}' \int dR dP \hat{\chi}_{wi} \hat{\rho}_W(R, P, t) \quad (90)$$

to linear order in the affinities. Assuming the time dependence of the affinities can be represented by a single Fourier component $\mathcal{A}_i(t) = \exp(i\omega t)\mathcal{A}_i(\omega)$, linear response theory gives

$$\frac{d\overline{\hat{\chi}_{wi}}(t)}{dt} = \sum_{j=1}^r \Phi_{ij}(\omega) \mathcal{A}_j(t) \quad (91)$$

where the one-sided Fourier transform of the matrix response function is given by

$$\Phi_{ij}(\omega) = \int_0^\infty dt \langle (\hat{\chi}_{wi}(t), \hat{\chi}_{wj}^\dagger) \rangle e^{-i\omega t} \quad (92)$$

Although the zero frequency limit of Eq. (91) has the same form as the phenomenological rate law (88), the zero frequency limit of Eq. (92) may be shown to be identically zero. This is the well-known plateau value problem, which is solved by using a projection operator formalism to project out the time variations that occur on the timescale of the chemical relaxation processes [6, 7]. Provided the timescales of the chemical relaxation processes, τ_c ,

are much slower than those for other microscopic relaxation processes in the system, τ_m , the phenomenological coefficients may be obtained through the correlation function expression,

$$\beta L_{ij} = - \int_0^{t^*} dt' \text{Tr}' \int dRdP \hat{\chi}_{wi}(t') (\hat{\chi}_{wj}^\dagger, \hat{\rho}_{we}) \quad (93)$$

where $\tau_m \ll t^* \ll \tau_c$. In writing this expression, we have moved the quantum-classical bracket to act on the equilibrium density and the initial value of the species operator. It is also convenient to define the time-dependent Onsager coefficients by

$$\begin{aligned} \beta L_{ij}(t) &= - \int_0^t dt' \text{Tr}' \int dRdP \hat{\chi}_{wi}(t') (\hat{\chi}_{wj}^\dagger, \hat{\rho}_{we}) \\ &= - \text{Tr}' \int dRdP \hat{\chi}_{wi}(t) (\hat{\chi}_{wj}^\dagger, \hat{\rho}_{we}) \end{aligned} \quad (94)$$

where the time integral has been performed to obtain the second line of this equation. The true phenomenological coefficients, appearing in Eq. (88), may be determined from the plateau value of this expression, should such a plateau exist. In quantum-classical dynamics the Onsager reciprocal relations are valid to $\mathcal{O}(\mu^2)$. This is a consequence of the fact that the quantum-classical bracket satisfies the Jacobi identity only to $\mathcal{O}(\mu^2)$ [73].

7.2. Two-Level Model for Transfer Reactions

Often many features of proton and electron transfer processes can be captured by simple two-level models. In this section, we show how the general reactive flux formalism may be specialized to a transfer reaction $A \rightleftharpoons B$ where excited states participate in the reaction.

To this end, we consider a two-level system coupled to a classical bath. In accord with the standard picture of reaction rates for such systems, the Hamiltonian operator, expressed in a diabatic basis $\{|\uparrow\rangle, |\downarrow\rangle\}$, is taken to have the form [73].

$$\mathbf{H} = \begin{bmatrix} V_n(R_0) + \hbar\gamma_0 R_0 & -\hbar\Omega \\ -\hbar\Omega & V_n(R_0) - \hbar\gamma_0 R_0 \end{bmatrix} + \left[\frac{P_0^2}{2M_0} + \sum_{j=0}^N \frac{P_j^2}{2M_j} + \sum_{j=1}^N \frac{M_j}{2} \omega_j^2 \left(R_j^2 - \frac{c_j}{M_j \omega_j^2} R_0 \right)^2 \right] \mathbf{I} \quad (95)$$

In this model, a two-level system is coupled to a classical nonlinear oscillator with mass M_0 and phase space coordinates (R_0, P_0) . The coupling to the two-level system is given by $-\hbar\gamma_0 R_0 = \hbar\gamma(R_0)$. The nonlinear quartic oscillator, $V_n(R_0) = aR_0^4/4 - bR_0^2/2$, is bilinearly coupled to a harmonic bath with Ohmic spectral density. From the structure of the first 2×2 matrix in Eq. (95), the diabatic energies are given by $E_{1,2}^d(R_0) = V_n(R_0) \pm \hbar\gamma_0 R_0$ and the coupling between the diabatic states is $-\hbar\Omega$. The N independent harmonic oscillators labeled $j = 1, \dots, N$ have masses M_j and frequencies ω_j . The bilinear coupling is characterized by a spectral density, $J(\omega) = \pi \sum_{j=1}^N (c_j^2 / (2M_j \omega_j^2)) \delta(\omega - \omega_j)$, of Ohmic type where [75, 76] $c_j = (\xi \hbar \omega_0 M_j)^{1/2} \omega_j$, $\omega_j = -\omega_c \ln(1 - j\omega_0/\omega_c)$ and $\omega_0 = \frac{\omega_c}{N} (1 - e^{-\omega_{\max}/\omega_c})$.

The adiabatic states are obtained by diagonalization of the two-level system hamiltonian (95) and are given by,

$$|1; R_0\rangle = \frac{1}{\mathcal{N}} [(1+G)|\uparrow\rangle + (1-G)|\downarrow\rangle] \quad (96)$$

$$|2; R_0\rangle = \frac{1}{\mathcal{N}} [-(1-G)|\uparrow\rangle + (1+G)|\downarrow\rangle] \quad (97)$$

where $\mathcal{N}(R_0) = \sqrt{2(1+G^2(R_0))}$ with $G(R_0) = \gamma(R_0)^{-1} [-\Omega + \sqrt{\Omega^2 + \gamma^2(R_0)}]$. In the following, we use the notation $(R, P) = (R_0, R_1, \dots, R_N, P_0, P_1, \dots, P_N)$ for the point in the $2(N+1)$ dimensional phase space of the model. The corresponding adiabatic energies are $E_{1,2}(R) = V_b(R) \mp \sqrt{\Omega^2 + \gamma^2(R_0)}$, where

$$V_b(R) = V_n(R_0) + \sum_{j=0}^N \frac{P_j^2}{2M_j} + \sum_{j=1}^N \frac{M_j}{2} \omega_j^2 \left(R_j^2 - \frac{c_j}{M_j \omega_j^2} R_0 \right)^2 \quad (98)$$

Insight into the nature of the reaction dynamics can be gained by considering the adiabatic free energies along the R_0 coordinate, $W_{1,2}(R_0)$, defined by

$$\begin{aligned} W_{1,2}(R_0) &= -\beta^{-1} \ln \left(\int \prod_{j=1}^N dR_j Z_{1,2}^{-1} e^{-\beta E_{1,2}(R)} \right) \\ &= \beta^{-1} \ln Z_{1,2} + V_n(R_0) \mp \sqrt{\Omega^2 + \gamma_0^2 R_0^2} \end{aligned} \quad (99)$$

where $Z_{1,2} = \int dR \exp[-\beta E_{1,2}(R)]$.

These free energy functions are plotted in Fig. 13. The ground state free energy profile has two minima corresponding to two stable states separated by a barrier at $R_0 = 0$.

We define the positive and negative values of R_0 with species A and B , respectively. Thus, we take for the species variables, $\hat{N}_A = \Theta(R_0)$ and $\hat{N}_B = \Theta(-R_0)$. The chemical reactions,



are described by the mass action rate law,

$$\frac{d\bar{n}_A(t)}{dt} = -k_{AB}\bar{n}_A(t) + k_{BA}\bar{n}_B(t) \quad (101)$$

which may also be written in the form

$$\frac{d\bar{n}_A(t)}{dt} = -k_{AB}\bar{n}_A(t)(1 - e^{-\beta \mathcal{A}(t)}) \quad (102)$$

by using the fact that the chemical potential of species α is $\mu_\alpha = \mu_\alpha^{(0)} + \beta^{-1} \ln \bar{n}_\alpha$ where $\alpha = A, B$. This form makes evident the fact that the driving force of the reaction is the chemical affinity $\mathcal{A}(t) = \mu_A(t) - \mu_B(t)$. If we linearize this rate law close to equilibrium, we obtain

$$\frac{d\bar{n}_A(t)}{dt} = -k_{AB}\bar{n}_A^{eq} \beta \mathcal{A}(t) \quad (103)$$

We may now read off the relation between the Onsager coefficient and the rate constant. We have,

$$L_{BA} = k_{AB}\bar{n}_A^{eq} \quad (104)$$

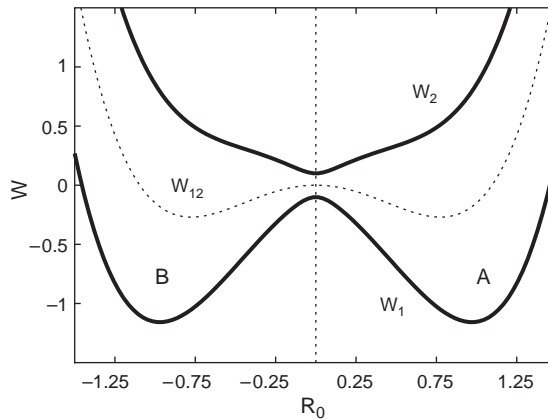


Figure 13. Free energy curves versus R_0 for the two-state model. The heavy solid lines are the ground and excited state free energy curves, and the light line depicts the mean of these curves.

Consider the calculation of $L_{BA}(\bar{n}_A^{eq})^{-1} = k_{AB}$. Using Eq. (94) and the definition (104), we have

$$\begin{aligned} k_{AB}(t) &= -(\beta\bar{n}_A^{eq})^{-1} \text{Tr}' \int dRdP \hat{\chi}_B(t)(\hat{\chi}_A, \hat{\rho}_{We}), \\ &= -(\beta\bar{n}_A^{eq})^{-1} \sum_{\alpha\alpha'} \int dRdP \chi_B^{\alpha\alpha'}(t)(\hat{\chi}_A, \hat{\rho}_{We})_{\alpha\alpha'} \end{aligned} \quad (105)$$

In the second line of this equation, we expressed the trace in terms of the adiabatic basis. This correlation function expression can be used to compute k_{AB} .

An expression for the time-dependent rate coefficient $k_{AB}(t)$ can be found by evaluating the matrix elements of the quantum-classical bracket in the adiabatic basis and using $\hat{N}_A^{\alpha\alpha'} = \delta_{\alpha\alpha'}\Theta(R_0)$ and $\hat{N}_B^{\alpha\alpha'} = \delta_{\alpha\alpha'}\Theta(-R_0)$. If we make use of the fact that the quantum-classical equilibrium density has the form,

$$\rho_{We}^{\alpha\alpha'} \approx \rho_{We}^{(0)\alpha} \delta_{\alpha\alpha'} - i\hbar f_{We}^{\alpha\alpha'} (1 - \delta_{\alpha\alpha'}) \quad (106)$$

where

$$\rho_{We}^{(0)\alpha} = Z_0^{-1} e^{-\beta H_W^\alpha}, \quad Z_0 = \sum_{\alpha} \int dRdP e^{-\beta H_W^\alpha} \quad (107)$$

and

$$f_{We}^{\alpha\alpha'} = \frac{P_0}{M_0} \cdot d_{\alpha\alpha'} \rho_{We}^{(0)\alpha} \left[\frac{\beta}{2} (1 + e^{-\beta E_{\alpha'\alpha}}) + \frac{1 - e^{-\beta E_{\alpha'\alpha}}}{E_{\alpha'\alpha}} \right] \quad (108)$$

the time-dependent rate coefficient in Eq. (105) can be decomposed into the sum of two contributions:

$$k_{AB}(t) = k_{AB}^d(t) + k_{AB}^o(t) \quad (109)$$

The diagonal part of the density matrix gives rise to the contribution

$$k_{AB}^d(t) = -\frac{1}{\bar{n}_A^{eq}} \sum_{\alpha=1}^2 \int dRdP N_B^{\alpha\alpha}(R, P, t) \delta(R_0) \frac{P_0}{M} \rho_{We}^{\alpha\alpha} \quad (110)$$

and the off-diagonal part of the density matrix yields

$$k_{AB}^o(t) = -\frac{2\hbar}{\beta\bar{n}_A^{eq}} \int dRdP \mathcal{I}m\{N_B^{12}(R, P, t)\} \delta(R_0) \frac{\partial f_{We}^{12}}{\partial P_0} \quad (111)$$

The rate coefficient can be calculated from the plateau value of $k_{AB}(t)$.

7.3. Two-Level Reaction Simulation Results

In this section, we present the results of simulations of the two-level reaction model to show how the nonadiabatic rate constant can be calculated in the context of quantum-classical Liouville dynamics. In presenting the results, we use a set of dimensionless coordinates $\tilde{R}_0 = (M_0\omega_c/\hbar)^{1/2}R_0$, $\tilde{P}_0 = (\hbar M_0\omega_c)^{-1/2}P_0$, $\tilde{R}_j = (M_j\omega_c/\hbar)^{1/2}R_j$ and $\tilde{P}_j = (\hbar M_j\omega_c)^{-1/2}P_j$, so that $\tilde{\hat{H}} = \hat{H}/(\hbar\omega_c)$, and the dimensionless parameters of the model are $\tilde{\Omega} = \Omega/\omega_c$, $\tilde{\omega}_j = \omega_j/\omega_c$, $\tilde{c}_j = (\xi\omega_0/\omega_c)^{1/2}\omega'_j$, $\tilde{a} = (\hbar/(M_0^2\omega_c^3))a$, $\tilde{b} = b/(M_0\omega_c^2)$, $\tilde{\gamma}_0 = (\hbar/M_0\omega_c^3)^{1/2}\gamma_0$, and $\tilde{\gamma}_b = (\hbar/M_0\omega_c)^{1/2}\gamma_b$. The dimensionless reciprocal temperature and time are $\tilde{\beta} = \hbar\omega_c\beta = \hbar\omega_c/k_B T$ and $\tilde{t} = t\omega_c$, respectively. In the following, the tilde will be omitted to avoid cluttering the notation, but the use of dimensionless units should be understood. Our calculations were carried out for a bath of $N = 100$ harmonic oscillators with the following values for the parameters: $\omega_{\max} = 3$, $\xi = 4$, $\Omega = 0.1$, $\gamma_0 = 1$, $a = 3$, $b = 1.8008$, and $\beta = 6$.

If the dynamics is restricted to the adiabatic ground state, the time evolution of $R_0(t)$ shown in Fig. 14 exhibits the features of an activated rate process between two metastable

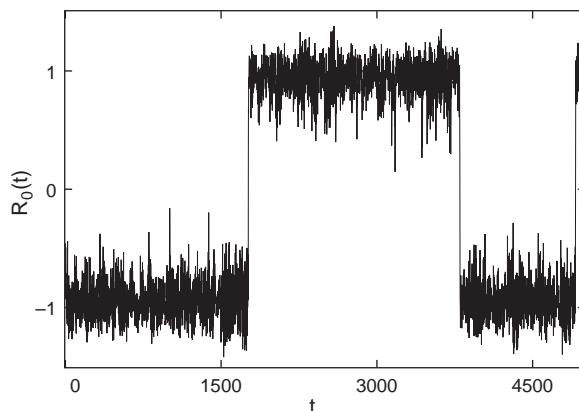


Figure 14. Time series of the coordinate $R_0(t)$ along a trajectory evolving on the ground state surface, typical of classical activated barrier crossing dynamics.

states. In the adiabatic limit, only the first term in Eq. (87) contributes, and the time-dependent rate coefficient in Eqs. (109) and (110) reduces to

$$k_{AB}^{ad}(t) = \frac{1}{\bar{n}_A^{eq}} \int dRdP (e^{iL_{11}t} \Theta(R_0)) \delta(R_0) \frac{P_0}{M_0} \rho_{We}^{11} \quad (112)$$

the standard reactive flux autocorrelation expression for a classical activated rate process. This adiabatic time-dependent rate coefficient is plotted in Fig. 15. It has an initial rapid decay followed by a much slower decay, which takes place on the timescale of the chemical rate process. The adiabatic rate constant can be determined from the extrapolation of this slowly decaying portion of the dynamics to $t = 0$.

In order to compute the nonadiabatic rate constant, we must calculate the contributions coming from the two terms in Eq. (109). The term $k_{AB}^d(t)$ in Eq. (110) involves even numbers of quantum transitions, whereas k_{AB}^o in Eq. (111) requires an odd number of transitions. Figure 16 shows the nonadiabatic transmission coefficient including both terms in Eq. (109) for up to two quantum transitions per trajectory. For this contribution, the trajectory starts at $t = 0$ from the ground state at the top of the barrier and evolves on the ground state surface until time τ_1 where a quantum transition occurs. Between the times τ_1 and τ_2 , evolution occurs on the mean surface. The jump at time τ_2 must bring the trajectory back either to the ground or to the excited state surface after which the evolution proceeds adiabatically until time t . Thus, one has three trajectory segments: the first and the last have no quantum phase factor but the middle trajectory segment has a nonzero phase factor arising from the coherent evolution on the mean surface $[E_1(R) + E_2(R)]/2$.

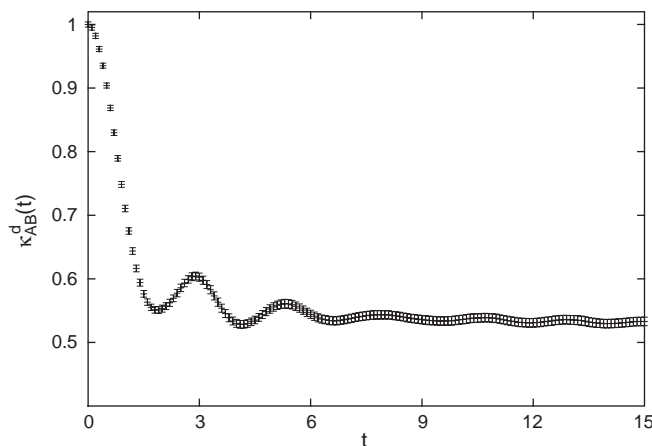


Figure 15. Transmission coefficient $\kappa_{AB}^d(t) = k_{AB}^d(t)/k_{AB}^{TST}$ versus time for adiabatic dynamics.

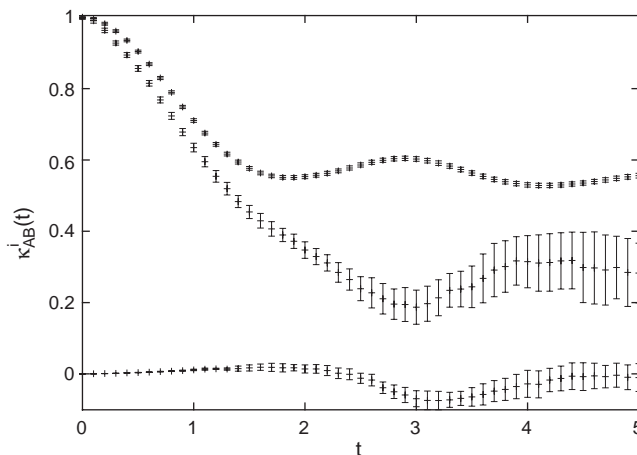


Figure 16. Time-dependent transmission coefficients $\kappa_{AB}^i(t) = k_{AB}(t)/k_{AB}^{TST}$. The lower curve shows the off-diagonal contribution (κ_{AB}^o). The middle curve arises from the sum of all the nonadiabatic corrections [$\kappa_{AB}^d(t) + \kappa_{AB}^o(t)$] considering up to two quantum transitions. For comparison, the upper curve shows the adiabatic result $\kappa_{AB}^{ad}(t)$.

Figure 16 shows also the nonadiabatic term $\kappa_{AB}^o(t) = k_{AB}^o/k_{AB}^{TST}$ versus time. Only odd numbers of nonadiabatic transitions contribute to this term. The contribution $k_{AB}^o(t)$ in Eq. (111) depends on the off-diagonal part of bracket $(\widehat{N}_A, \widehat{\rho}_{We})_{\alpha\alpha'}$ and the off-diagonal part of the species variable $N_B^{\alpha'\alpha}(t)$, ($\alpha \neq \alpha'$). One can see that this off-diagonal term gives a negligible contribution so that the main physics is contained in $k_{AB}^d(t)$. Finally, the full time-dependent rate constant in Fig. 16 shows that the inclusion of nonadiabatic transitions significantly reduces the rate constant below that obtained using adiabatic dynamics.

8. CONCLUSIONS

The rates of proton and electron transfer reactions in condensed phase environments are difficult to determine because the quantum nature of the transferring particle must be taken into account. In most circumstances, we can use a mixed quantum-classical approach to study such reactions because solvent molecules are typically much heavier than the proton or electron being transferred in the reaction. Equilibrium properties such as the free energy along the reaction coordinate may be computed using Feynman path integral methods. The free energy provides information on the reaction mechanism and is an important ingredient in the transition state theory approximation to the rate constant. Dynamical properties, such as the full rate constant, are much more difficult to compute. Mixed quantum-classical dynamical schemes may be used to determine transport properties. Adiabatic dynamics, where the motion of the classical degrees of freedom takes place on a single potential energy surface, is the simplest such scheme. However, this approach breaks down when transitions among the quantum states take place. In this case, nonadiabatic dynamics must be used. The quantum-classical Liouville equation and the associated statistical mechanical derivation of the nonadiabatic reactive flux formula for the rate of the reaction provide a way to study nonadiabatic proton and electron transfer rates.

If charge transfer reactions take place in domains with nanometer dimensions, then the competition between bulk and surface forces leads to interesting effects on reaction mechanisms and rates. Our examples of electron solvation in reverse micelles and proton transfer in polar molecule clusters served to illustrate such effects.

ACKNOWLEDGMENTS

This work was supported in part by a grant from the Natural Sciences and Engineering Research Council of Canada.

REFERENCES

1. M. D. Joesten and L. J. Schaad, "Hydrogen Bonding." Marcel-Decker, New York, 1974.
2. R. P. Bell, "The Proton in Chemistry." Chapman & Hall, London, 1973.
3. J. Ulstrup, "Charge Transfer Processes." Springer, New York, 1979.
4. T. Yamamoto, *J. Chem. Phys.* 33, 281 (1960).
5. D. Chandler, *J. Chem. Phys.* 68, 472 (1978).
6. S. Consta, R. Kapral, and L. McWhirter, in "Classical and Quantum Dynamics in the Condensed Phase" (G. Ciccotti, B. Berne, and D. Coker, Eds.), p. 583. World Scientific, Singapore, 1998.
7. R. Kapral, *J. Chem. Phys.* 56, 1842 (1972).
8. F. Garisto and R. Kapral, *J. Chem. Phys.* 58, 3129 (1973).
9. H. Mori, *Prog. Theor. Phys.* 33, 423 (1965).
10. R. Zwanzig, *Phys. Rev.* 124, 983 (1961).
11. R. Kubo, *J. Phys. Soc. (Japan)* 12, 570 (1957); *Repts. Prog. Phys.* 29, 255 (1966).
12. W. E and E. Vanden-Eijnden, "Metastability, Conformational Dynamics, and Transition Pathways in Complex Systems, in Multiscale Modelling and Simulation" (S. Attinger and P. Koumoutsakos, Eds.), Lecture Notes in Computational Science and Engineering, Vol. 39. Springer, Berlin, 2004.
13. W. E, W. Ren, and E. Vanden-Eijnden, "Finite Temperature String Method for the Study of Rare Events," *J. Phys. Chem. B* (submitted).
14. H. Jónsson, G. Mills, and K. W. Jacobsen, in "Classical and Quantum Dynamics in Condensed Phase Simulations" (B. J. Berne, G. Ciccotti, and D. F. Coker, Eds.). World Scientific, Singapore, 1998.
15. R. Elber, A. Ghosh, and A. Cardenas, *Acc. Chem. Res.* 35, 396 (2002).
16. C. Dellago, P. G. Bolhuis, and P. L. Geissler, *Adv. Chem. Phys.* 123, 1 (2002).
17. E. Carter, G. Ciccotti, J. T. Hynes, and R. Kapral, *Chem. Phys. Lett.* 156, 472 (1989).
18. M. Fixman, *Proc. Natl. Acad. Sci. U.S.A.* 71, 3050 (1974).
19. N. G. van Kampen, *Am. J. Phys.* 52, 419 (1984).
20. H. Goldstein, "Classical Mechanics." Addison-Wesley Reading, MA, 1980.
21. M. Sprik and G. Ciccotti, *J. Chem. Phys.* 109, 7737 (1998).
22. R. P. Feynman, "Statistical Mechanics." Addison-Wesley, Reading MA, 1972.
23. D. Chandler and P. G. Wolynes, *J. Chem. Phys.* 74, 4078 (1981).
24. M. Gillan, *J. Phys. C* 20, 3621 (1987).
25. G. A. Voth, *Adv. Chem. Phys.* 93, 135 (1996).
26. D. Laria and R. Kapral, *J. Chem. Phys.* 117, 7712 (2002).
27. P. L. Luisi and B. E. Straub, Eds., "Reverse Micelles." Plenum, New York, 1984.
28. M. P. Peltini, Ed., "Structure and Reactivity in Reverse Micelles." Elsevier, Amsterdam, 1989.
29. B. Derecskei, A. Derecskei-Kovacs, and Z. A. Schelly, *Langmuir* 15, 1981 (1999).
30. J. Faeder and B. Ladanyi, *J. Phys. Chem. B* 104, 1033 (2000); *J. Phys. Chem. B* 105, 11148 (2001).
31. J. Schnitker and P. J. Rossky, *J. Chem. Phys.* 86, 3462 (1987).
32. G. B. Bachelet, D. R. Hamann, and M. Schlüter, *Phys. Rev. B* 26, 4199 (1982).
33. H. J. C. Berendsen, J. R. Grigera, and T. P. Straatsma, *J. Phys. Chem.* 91, 6269 (1987).
34. M. Tuckerman, G. J. Martyna, and B. J. Berne, *J. Chem. Phys.* 97, 1990 (1992).
35. G. J. Martyna, M. E. Tuckerman, D. J. Tobias, and M. L. Klein, *Mol. Phys.* 87, 1117 (1996).
36. G. J. Martyna, M. L. Klein, and M. Tuckerman, *J. Chem. Phys.* 97, 2635 (1992).
37. J. P. Ryckaert, G. Ciccotti, and H. J. C. Berendsen, *J. Comp. Phys.* 23, 327 (1977); G. Ciccotti and J. P. Ryckaert, *Comp. Phys. Rep.* 4, 345 (1986).
38. S. Consta and R. Kapral, *J. Chem. Phys.* 101, 10908 (1994).
39. S. Nosé, *Mol. Phys.* 52, 255 (1984); *J. Chem. Phys.* 81, 511 (1984); *Mol. Phys.* 57, 187 (1986); *Prog. Theor. Phys. Suppl.* 103, 1 (1991).
40. W. Hoover, *Phys. Rev. A* 31, 1695 (1985).
41. D. Laria, G. Ciccotti, M. Ferrario, and R. Kapral, *Chem. Phys.* 180, 181 (1994).
42. D. Li and G. Voth, *J. Phys. Chem.* 95, 10425 (1991).
43. J. Lobaugh and G. Voth, *Chem. Phys. Lett.* 198, 311 (1992); *J. Chem. Phys.* 100, 3039 (1994).
44. D. Laria, G. Ciccotti, M. Ferrario, and R. Kapral, *J. Chem. Phys.* 97, 378 (1992).
45. D. C. Borgis, S. Lee, and J. T. Hynes, *Chem. Phys. Lett.* 19, 162 (1989); D. C. Borgis and J. T. Hynes, *J. Chem. Phys.* 94, 3619 (1991).
46. R. A. Marcus and N. Sutin, *Biochim. Biophys. Acta* 811, 265 (1985).
47. A. Warshel, *J. Am. Chem. Soc.* 86, 2218 (1982).
48. D. A. Zichi, G. Ciccotti, J. T. Hynes, and M. Ferrario, *J. Phys. Chem.* 93, 6261 (1989).
49. H. Azzouz and D. C. Borgis, *J. Chem. Phys.* 98, 7361 (1993).
50. E. Wigner, *Phys. Rev.* 40, 749 (1932).
51. K. Imre, E. Özizmir, M. Rosenbaum, and P. F. Zwiefel, *J. Math. Phys.* 5, 1097 (1967)
52. R. Kapral and G. Ciccotti, *J. Chem. Phys.* 110, 8919 (1999).
53. S. Consta and R. Kapral, *J. Chem. Phys.* 104, 4581 (1996).
54. A. S. Clarke, R. Kapral, B. Moore, G. Patey, and X.-G. Wu, *Phys. Rev. Lett.* 70, 3283 (1993); A. S. Clarke, R. Kapral, and G. N. Patey, *J. Chem. Phys.* 101, 2432 (1994).
55. J. C. Tully, "Modern Methods for Multidimensional Dynamics Computations in Chemistry" (D. L. Thompson, Ed.), p. 34. World Scientific, NY, 1998.

56. H. J. Berendsen and J. Mavri, *J. Phys. Chem.* 97, 13464 (1993).
57. P. Bala, B. Lesyng, and J. A. McCammon, *Chem. Phys. Lett.* 219, 259 (1994).
58. J. C. Tully, *J. Chem. Phys.* 93, 1061 (1990); J. C. Tully, *Int. J. Quantum Chem.* 25, 299 (1991); S. Hammes-Schiffer and J. C. Tully, *J. Chem. Phys.* 101, 4657 (1994).
59. P. Pechukas, *Phys. Rev.* 181, 166, 174 (1969).
60. F. Webster, P. J. Rossky, and P. A. Friesner, *Comp. Phys. Comm.* 63, 494 (1991); F. Webster, E. T. Wang, P. J. Rossky, and P. A. Friesner, *J. Chem. Phys.* 100, 483 (1994).
61. L. Xiao and D. F. Coker, *J. Chem. Phys.* 100, 8646 (1994); D. F. Coker and L. Xiao, *J. Chem. Phys.* 102, 496 (1995); H. S. Mei and D. F. Coker, *J. Chem. Phys.* 104, 4755 (1996).
62. S. Hammes-Schiffer and J. C. Tully, *J. Chem. Phys.* 103, 8528 (1995).
63. S. R. Billeter, S. P. Webb, T. Iordanov, P. K. Agarwal, and S. Hammes-Schiffer, *J. Chem. Phys.* 114, 6925 (2001).
64. V. I. Gerasimenko, *Repts. Ukrainian Acad. Sci.* 10, 65 (1981); V. I. Gerasimenko: *Theor. Math. Phys.* 50, 77 (1982); D. Ya. Petrina, V. I. Gerasimenko, and V. Z. Enolskii, *Sov. Phys. Dokl.* 35, 925 (1990).
65. I. V. Aleksandrov, *Z. Naturforsch.* 36a, 902 (1981).
66. W. Boucher and J. Traschen, *Phys. Rev. D* 37, 3522 (1988).
67. W. Y. Zhang and R. Balescu, *J. Plasma Phys.* 40, 199 (1988); R. Balescu and W. Y. Zhang, *J. Plasma Phys.* 40, 215 (1988).
68. C. C. Martens and J.-Y. Fang, *J. Chem. Phys.* 106, 4918 (1996); A. Donoso and C. C. Martens, *J. Phys. Chem.* 102, 4291 (1998).
69. S. Nielsen, R. Kapral, and G. Ciccotti, *J. Chem. Phys.* 115, 5805 (2001).
70. R. Kapral and G. Ciccotti, "A Statistical Mechanical Theory of Quantum Dynamics in Classical Environments, in Bridging Time Scales: Molecular Simulations for the Next Decade" (P. Nielaba, M. Mareschal, and G. Ciccotti, Eds.), SIMU Conference, 2001. Springer, Berlin, 2003.
71. D. Mac Kernan, G. Ciccotti, and R. Kapral, *J. Phys.: Condens. Matt.* 14, 9069 (2002).
72. A. Sergi, D. Mac Kernan, G. Ciccotti, and R. Kapral, *Theor. Chem. Acc.* 110, 49 (2003).
73. A. Sergi and R. Kapral, *J. Chem. Phys.* 118, 8566 (2003).
74. S. R. de Groot and P. Mazur, "Non-Equilibrium Thermodynamics." North-Holland, Amsterdam, 1962.
75. N. Makri and K. Thompson, *Chem. Phys. Lett.* 291, 101 (1998); K. Thompson and N. Makri, *J. Chem. Phys.* 110, 1343 (1999); N. Makri, *J. Phys. Chem. B* 103, 2823 (1999).
76. D. Mac Kernan, R. Kapral, and G. Ciccotti, *J. Chem. Phys.* 116, 2346 (2002).